Janet D. Scheel, Mohammad S. Emran and Jörg Schumacher

Resolving the fine-scale structure in turbulent Rayleigh-Bénard convection

Original published in:

In: New journal of physics : the open-access journal for physics. - [Bad Honnef] : Dt. Physikalische Ges. - Bd. 15.2013 (Nov.), 113063, insges. 32 S.

Original published: 2013-11-29
ISSN (online): 1367-2630
DOI: 10.1088/1367-2630/15/11/113063
URL: http://dx.doi.org/10.1088/1367-2630/15/11/113063
[*Visited:* 2016-09-15]

New Journal of Physics
The open access journal for physics

Resolving the fine-scale structure in turbulent Rayleigh–Bénard convection

Janet D Scheel[1], **Mohammad S Emran**[2] **and Jörg Schumacher**[2]
[1] Department of Physics, Occidental College, Los Angeles, CA 90041, USA
[2] Institut für Thermo- und Fluiddynamik, Postfach 100565, Technische Universität Ilmenau, D-98684 Ilmenau, Germany
E-mail: jscheel@oxy.edu, mohammad-shah.emran@tu-ilmenau.de and joerg.schumacher@tu-ilmenau.de

New Journal of Physics **15** (2013) 113063 (32pp)
Received 23 July 2013
Published 29 November 2013
Online at http://www.njp.org/
doi:10.1088/1367-2630/15/11/113063

Abstract. We present high-resolution direct numerical simulation studies of turbulent Rayleigh–Bénard convection in a closed cylindrical cell with an aspect ratio of one. The focus of our analysis is on the finest scales of convective turbulence, in particular the statistics of the kinetic energy and thermal dissipation rates in the bulk and the whole cell. The fluctuations of the energy dissipation field can directly be translated into a fluctuating local dissipation scale which is found to develop ever finer fluctuations with increasing Rayleigh number. The range of these scales as well as the probability of high-amplitude dissipation events decreases with increasing Prandtl number. In addition, we examine the joint statistics of the two dissipation fields and the consequences of high-amplitude events. We have also investigated the convergence properties of our spectral element method and have found that both dissipation fields are very sensitive to insufficient resolution. We demonstrate that global transport properties, such as the Nusselt number, and the energy balances are partly insensitive to insufficient resolution and yield correct results even when the dissipation fields are under-resolved. Our present numerical framework is also compared with high-resolution simulations which use a finite difference method. For most of the compared quantities the agreement is found to be satisfactory.

Contents

1. Introduction

Turbulent fluid motion in nature and technology is frequently driven by sustained temperature differences [5]. Applications range from cooling devices of chips to convection in the Earth and the Sun. Turbulent Rayleigh–Bénard convection (RBC) is the paradigm for all these convective phenomena because it can be studied in a controlled manner, but it still has enough complexity to contain the key features of convective turbulence in the examples just mentioned. RBC in cylindrical cells has been studied intensely over the last few years in several laboratory experiments, mostly in slender cells of aspect ratio smaller than or equal to unity in order to reach the largest possible Rayleigh numbers or to resolve the detailed mechanisms of turbulent heat transport close to the walls [1, 5]. Direct numerical simulations have also grown such that the detailed dynamical and statistical aspects of the involved turbulent fields and their characteristic structures can now be unraveled in detail.

The key question in RBC is the mechanism of turbulent transport of heat and momentum. Since the fluid motion is driven by a constant temperature difference between the top and bottom plates, thin boundary layers of temperature and velocity will form on these walls as well as on the side walls of the cell. A deeper understanding of the global transport mechanisms is possible only if we understand the dynamical coupling between the boundary layers and the rest of the flow in the bulk of the cell. While the boundary layers are strongly dominated by the presence of mean gradients of the temperature and velocity fields, the bulk of the convection layer is well mixed by the turbulence such that mean gradients of the involved turbulent fields remain subdominant compared to the local fluctuations. The flow at hand is thus strongly inhomogeneous, at least in the vertical direction, so it can be expected that the smallest dynamically relevant scales will differ when moving from the isothermal walls to the bulk.

Central to our understanding of the statistics of the turbulent transport is the role of the gradient fields of velocity and temperature which fluctuate extremely strongly at the

small scales of the flow. This is a unique property of all turbulent flows. Dissipation rate fields—which measure the magnitude of these gradient fluctuations and are still inaccessible in experiments with respect to their three-dimensional structure [36]—are thus at the core of a deeper understanding of turbulence as a whole.

In the present work we want to make a further step forward with direct numerical simulations (DNS) of RBC by resolving fine scales never accessed before, both in the bulk and boundary layers, in order to study the statistics of the gradient fields, their joint extreme events, the statistical effect of rare high-amplitude events as well as Rayleigh and Prandtl number variation. A spectral element method (SEM) is used to conduct the numerical studies [9, 10]. It combines the flexibility in terms of mesh geometry that is inherent to every finite element method with the exponentially fast convergence of a spectral method. We will show that several tests which have been applied in DNS in the past are insensitive with respect to insufficient resolution. These tests, which are based on global averages of mean dissipation rates and the global mean heat fluxes, give correct results although the fine-scale structure of the turbulence is still under-resolved particularly in the bulk of the convection cell. In order to address these questions in detail we will present a comprehensive statistical analysis of the temperature and velocity gradient fields, in particular the related dissipation rates and dissipation scales.

It is crucial to resolve all the dynamically important scales to represent the flow faithfully when carrying out DNS which involve no subgrid-scale parametrization. Several attempts have been made in order to derive resolution criteria starting with the pioneering work by Grötzbach [16], subsequent refinements of this criterion [2, 27, 31] and works with a focus to the fine resolution of the boundary layer dynamics [21, 26, 35]. Only recently the focus of DNS studies was shifted toward the bulk in a cubic convection cell [17] with a discussion of the scaling properties and statistics of the dissipation fields.

It is well-known that the gradients of the turbulent fields are most sensitive to insufficient resolution. Superfine resolution simulations in isothermal box turbulence [23–25] and in turbulent shear flows [14] have led to some enlightening results on the distribution of the finest scales in such flows and their relation to the small-scale intermittency. This intermittency is known to be coupled tightly to two highly fluctuating dissipation rates, one of the kinetic energy and the other of the thermal variance. The thermal dissipation rate is defined as

$$\epsilon_T(\mathbf{x}, t) = \kappa(\nabla T)^2, \tag{1}$$

where $T(\boldsymbol{x}, t)$ is the temperature field and κ the thermal diffusivity. The kinetic energy dissipation rate is defined as

$$\epsilon(\mathbf{x}, t) = \frac{\nu}{2}\left(\nabla \boldsymbol{u} + \nabla \boldsymbol{u}^{\mathrm{T}}\right)^2, \tag{2}$$

with the turbulent velocity field $\boldsymbol{u}(\mathbf{x}, t)$ and the kinematic viscosity ν. The mean kinetic energy dissipation rate $\langle\epsilon\rangle$ is related to the mean Kolmogorov scale $\langle\eta_{\mathrm{K}}\rangle$ which is the smallest mean scale when $\nu \leqslant \kappa$. The symbol $\langle\cdot\rangle$ denotes an ensemble average which is calculated in numerical simulations as a volume–time average. In case of $\nu > \kappa$, the smallest mean scale is determined by the (active) scalar field known as the Batchelor scale [3], $\langle\eta_{\mathrm{B}}\rangle$. Both scales are defined as

$$\langle\eta_{\mathrm{K}}\rangle = \frac{\nu^{3/4}}{\langle\epsilon\rangle^{1/4}} \quad \text{and} \quad \langle\eta_{\mathrm{B}}\rangle = \frac{\langle\eta_{\mathrm{K}}\rangle}{\sqrt{Pr}}. \tag{3}$$

Here, Pr is the Prandtl number and given by

$$Pr = \frac{\nu}{\kappa}. \tag{4}$$

Both dissipation fields can be expected to fluctuate strongly exceeding their means by orders of magnitude [23, 29]. Therefore it was suggested to generalize the classical dissipation and diffusion scales to local dissipation and diffusion scales [22, 30] which are given by (see also a discussion in Hamlington *et al* [14])

$$\eta_{\mathrm{K}}(\mathbf{x},t)=\frac{\nu^{3/4}}{\epsilon(\mathbf{x},t)^{1/4}}\quad\text{and}\quad\eta_{\mathrm{B}}(\mathbf{x},t)=\frac{\eta_{\mathrm{K}}(\mathbf{x},t)}{\sqrt{Pr}}. \tag{5}$$

Both scales will pick up the highly intermittent fluctuations of the dissipation rates and can thus not only become smaller but also larger than the mean scales which were defined in (3). Local dissipation scales have been studied in convection experiments by Zhou and Xia [41]. One main finding was that the distribution of the scales can be described by the same tools as in isothermal box turbulence. In the present work we will also access these scales and compare their distribution in different parts of the convection cell.

The paper is organized as follows. In section 2, we will discuss in brief the equations of motion and some central relations which will become necessary for our data analysis. Furthermore we briefly review the existing resolution criteria. First it is shown that global balance equation checks are insensitive to insufficient resolution. We also compare the results with a second-order finite difference method (FDM) [33, 34] which has been one workhorse in RBC over the past decade. In section 3 we report our results. We study the statistics of the dissipation rate fields and calculate the local dissipation scales. Then we present a comparison of dissipation rate fields and scales as a function of Rayleigh number and Prandtl number using our very highest resolution. We summarize our findings and give a brief outlook at the end.

2. Equations of motion and numerical method

2.1. Boussinesq equations and further non-dimensional relations

We solve the three-dimensional Boussinesq equations numerically. The height of the cell H, the free-fall velocity $U_{\mathrm{f}}=\sqrt{g\alpha\Delta T H}$ and the imposed temperature difference ΔT are used to rescale the equations of motion. The three control parameters of RBC are the Rayleigh number Ra, the Prandtl number Pr and the aspect ratio $\Gamma=D/H$ with the diameter D. This results in the following dimensionless form of the equations of motion:

$$\tilde{\boldsymbol{\nabla}}\cdot\tilde{\mathbf{u}}=0, \tag{6}$$

$$\frac{\partial\tilde{\boldsymbol{u}}}{\partial\tilde{t}}+(\tilde{\boldsymbol{u}}\cdot\tilde{\boldsymbol{\nabla}})\tilde{\boldsymbol{u}}=-\tilde{\boldsymbol{\nabla}}\tilde{p}+\sqrt{\frac{Pr}{Ra}}\tilde{\boldsymbol{\nabla}}^2\tilde{\boldsymbol{u}}+\tilde{T}\mathbf{e}_z, \tag{7}$$

$$\frac{\partial\tilde{T}}{\partial\tilde{t}}+(\tilde{\mathbf{u}}\cdot\tilde{\boldsymbol{\nabla}})\tilde{T}=\frac{1}{\sqrt{Ra\ Pr}}\tilde{\boldsymbol{\nabla}}^2\tilde{T}, \tag{8}$$

where

$$Ra=\frac{g\alpha\Delta T H^3}{\nu\kappa}. \tag{9}$$

The variable g stands for the acceleration due to gravity and α is the thermal expansion coefficient. Throughout the study we set $\Gamma=1$. Times are measured in free-fall time units, $T_{\mathrm{f}}=\sqrt{H/(g\alpha\Delta T)}$. At all walls of the simulation volume V no-slip boundary conditions for

the fluid are applied, $\tilde{\boldsymbol{u}} = 0$. The side walls are adiabatic, i.e. the normal derivative of the temperature field vanishes, $\partial\tilde{T}/\partial\mathbf{n} = 0$. The top and bottom plates are held at fixed temperatures $\tilde{T} = 0$ and 1, respectively. In response to the input parameters Ra, Pr and Γ, a turbulent heat flux from the bottom to the top plate is established. It is determined by the Nusselt number which is defined as

$$Nu(\tilde{z}) = \sqrt{Ra\ Pr}\,\langle\tilde{u}_z\tilde{T}\rangle_{A,t} - \frac{\partial\langle\tilde{T}\rangle_{A,t}}{\partial\tilde{z}}. \tag{10}$$

Based on the volume average, we find $Nu_{\mathrm{V}} = 1 + \sqrt{Ra\ Pr}\langle\tilde{u}_z\tilde{T}\rangle_{V,t}$ which has to equal $Nu(\tilde{z})$ for all $\tilde{z} \in [0, 1]$. The non-dimensional expressions for the two dissipation rate fields, $\epsilon(\boldsymbol{x}, t)$ and $\epsilon_T(\boldsymbol{x}, t)$ are given by the following expressions:

$$\epsilon_T(\mathbf{x}, t) = \kappa\frac{(\Delta T)^2}{H^2}(\tilde{\boldsymbol{\nabla}}\tilde{T})^2 = \frac{(\Delta T)^2 U_{\mathrm{f}}}{H}\frac{1}{\sqrt{Ra\ Pr}}(\tilde{\boldsymbol{\nabla}}\tilde{T})^2 \tag{11}$$

and thus

$$\tilde{\epsilon}_T(\tilde{\boldsymbol{x}}, \tilde{t}) \equiv \frac{\epsilon_T(\mathbf{x}, t)H}{U_{\mathrm{f}}(\Delta T)^2} = \frac{1}{\sqrt{Ra\ Pr}}(\tilde{\boldsymbol{\nabla}}\tilde{T})^2. \tag{12}$$

The kinetic energy dissipation rate is defined as

$$\epsilon(\mathbf{x}, t) = \frac{\nu}{2}\frac{U_{\mathrm{f}}^2}{H^2}\left(\tilde{\boldsymbol{\nabla}}\tilde{\boldsymbol{u}} + \tilde{\boldsymbol{\nabla}}\tilde{\boldsymbol{u}}^{\mathrm{T}}\right)^2 = \frac{U_{\mathrm{f}}^3}{2H}\sqrt{\frac{Pr}{Ra}}\left(\tilde{\boldsymbol{\nabla}}\tilde{\boldsymbol{u}} + \tilde{\boldsymbol{\nabla}}\tilde{\boldsymbol{u}}^{\mathrm{T}}\right)^2 \tag{13}$$

and thus

$$\tilde{\epsilon}(\tilde{\boldsymbol{x}}, \tilde{t}) \equiv \frac{\epsilon(\mathbf{x}, t)H}{U_{\mathrm{f}}^3} = \frac{1}{2}\sqrt{\frac{Pr}{Ra}}\left(\tilde{\boldsymbol{\nabla}}\tilde{\boldsymbol{u}} + \tilde{\boldsymbol{\nabla}}\tilde{\boldsymbol{u}}^{\mathrm{T}}\right)^2. \tag{14}$$

Using equation (5) gives

$$\tilde{\eta}_{\mathrm{K}}(\tilde{\boldsymbol{x}}, \tilde{t}) \equiv \frac{\eta_{\mathrm{K}}(\tilde{\mathbf{x}}, \tilde{t})}{H} = \left[\frac{\nu^{3/4}}{(U_{\mathrm{f}}H)^{3/4}}\right]\tilde{\epsilon}(\tilde{\boldsymbol{x}}, \tilde{t})^{-1/4} = \frac{Pr^{3/8}}{Ra^{3/8}}\tilde{\epsilon}(\tilde{\boldsymbol{x}}, \tilde{t})^{-1/4} \tag{15}$$

for the cases of $Pr \leqslant 1$. To simplify (15) we used the definition of the Grashof number $Gr = (U_{\mathrm{f}}H)^2/\nu^2 = Ra/Pr$. The Batchelor scale follows as

$$\tilde{\eta}_{\mathrm{B}}(\tilde{\boldsymbol{x}}, \tilde{t}) \equiv \frac{\eta_{\mathrm{B}}(\tilde{\boldsymbol{x}}, \tilde{t})}{H} = \frac{1}{Pr^{1/8}Ra^{3/8}}\tilde{\epsilon}(\tilde{\boldsymbol{x}}, \tilde{t})^{-1/4} \tag{16}$$

for $Pr > 1$. For completeness, we also list two exact relations that can be derived from the balances of the turbulent kinetic energy and the scalar variance. They are given by [28]

$$\langle\tilde{\epsilon}_T\rangle_{V,t} = \frac{Nu}{\sqrt{Ra\ Pr}} \quad \text{and} \quad \langle\tilde{\epsilon}\rangle_{V,t} = \frac{Nu - 1}{\sqrt{Ra\ Pr}}. \tag{17}$$

If we make use of (17), equations (15) and (16) translate to

$$\langle\tilde{\eta}_{\mathrm{K}}\rangle = \left(\frac{Pr^2}{(Nu - 1)Ra}\right)^{\frac{1}{4}} \quad \text{and} \quad \langle\tilde{\eta}_{\mathrm{B}}\rangle = \left(\frac{1}{(Nu - 1)Ra}\right)^{\frac{1}{4}}. \tag{18}$$

Similar to the studies by Stevens *et al* [31], we will use equations (17) to test different grid resolutions at a given set of parameters and define relative errors that measure the difference between the left and right hand sides of equations (17) [3]

$$\Lambda_T = \frac{\sqrt{Ra\ Pr}\langle\tilde{\epsilon}_T\rangle_{V,t} - Nu}{Nu} \quad \text{and} \quad \Lambda_v = \frac{\sqrt{Ra\ Pr}\langle\tilde{\epsilon}\rangle_{V,t} - (Nu-1)}{Nu-1}. \tag{19}$$

In the following, we will continue with the dimensionless quantities and omit the tildes for convenience.

2.2. Numerical methods

For the DNS studies in the present work two different numerical methods are used and compared, a second-order finite difference scheme and a SEM.

2.2.1. Finite difference method. The Boussinesq equations (6)–(8) are discretized on a staggered grid with a second-order FDM which was developed by Verzicco and Orlandi [33, 34]. The pressure field p is determined by a two-dimensional Poisson solver after applying a one-dimensional fast Fourier transform in the azimuthal direction. The time advancement is done by a third-order Runge–Kutta scheme. The grid spacings are non-equidistant in the radial and vertical directions. In the vertical direction, the grid spacing is close to Tschebycheff collocation points. The simulation code is parallelized with MPI in combination with OpenMP.

2.2.2. Spectral element method. The equations are numerically solved by a SEM [9] which has been adapted to our problem. The code employs second order time-stepping, using the backward difference formula BDF2 which results at time step n and for a step width δt in the following set of discrete equations (see also equations (6)–(8)):

$$\hat{D}\boldsymbol{u}^n = 0, \tag{20}$$

$$\sqrt{\frac{Pr}{Ra}}\hat{A}\boldsymbol{u}^n + \frac{3}{2\delta t}\hat{B}\boldsymbol{u}^n + \nabla p^n = \boldsymbol{f}_u^n, \tag{21}$$

$$\frac{1}{\sqrt{Ra\ Pr}}\hat{A}T^n + \frac{3}{2\delta t}\hat{B}T^n = f_T^n \tag{22}$$

with the corresponding boundary conditions. Here, $\hat{D}$ is the divergence operator and $\hat{A}$ the stiffness matrix which contains the Laplace terms. The quantity $\hat{B}$ is the mass matrix which will contain the Gauss–Lobatto–Legendre (GLL) weights and the determinants of the Jacobian caused by the mapping to the deformed elements as diagonal entries. In order to arrive at (20)–(22) the Boussinesq equations are transformed into a weak formulation similar to other Galerkin methods. They are then discretized with the particular choice of spectral basis functions [6] which will be given further below. These basis functions allow for an exact evaluation of the integrals in the scalar products on the basis of the Gauss integration theorem. All flow fields are given in the Sobolev space $H^1(V)$ in which the functions and their derivatives are square integrable. For this space it holds that $C^1(V) \subset H^1(V) \subset C^0(V)$ [6]. The right hand

[3] Note that the relative errors are fairly sensitive to the averaging time because of the large fluctuations in Nusselt number that can occur for these turbulent systems.

sides, $\boldsymbol{f}_u^n$ and f_T^n of equations (22), incorporate remaining terms from the BDF2 time derivative, the nonlinear convection which is obtained by second-order extrapolation from steps $n-1$ and $n-2$, and the buoyancy.

The resulting linear, symmetric Stokes problem is solved implicitly. This system is split, decoupling the viscous and pressure steps into independent symmetric positive definite subproblems which are solved either by Jacobi (viscous) or multilevel Schwartz (pressure) preconditioned conjugate gradient iteration. Fast parallel solvers based on direct projection [32] or more scalable algebraic multigrid [12] are used for the coarse-grid solve that is part of the pressure preconditioner. For stabilization of the SEM, we perform de-aliasing by the use of over-integration of the convective term by a factor of either $N+5$ or $3(N+1)/2$, where N is the polynomial order. We also filter out 5% of the energy in the Nth mode for additional stabilization (see [11] for further information).

The basis functions $\psi_k(x)$ are Lagrangian interpolation polynomials of order N and composed of Legendre polynomials L_k for the present study. They are given by

$$\psi_k(x) = -\frac{1}{N(N+1)} \frac{(1-x^2)L'_N(x)}{(x-\xi_k)L_N(\xi_k)} \tag{23}$$

with the GLL points ξ_k. In contrast to a classical spectral or pseudospectral method the evaluation of spatial derivatives translates into matrix multiplications which have to be highly optimized (see the appendix for further details). The expansion in the three-dimensional case with a reference element $\Omega = [-1, 1]^3$ is based on the tensor product formulation of the basis functions

$$\mathbf{u}_e(x, y, z) = \sum_{i=0}^{N} \sum_{j=0}^{N} \sum_{k=0}^{N} \mathbf{u}(\xi_i, \xi_j, \xi_k)\ \psi_i(x) \otimes \psi_j(y) \otimes \psi_k(z). \tag{24}$$

In the simulation the elements that sum up to the volume V are deformed. Hence an additional mapping (Jacobian) from the reference element to all elements needs to be incorporated. Clearly, the mapping of the coordinates and the matching of the velocity and temperature fields between elements enhances the numerical effort in comparison to the second order FDM. We estimated that production runs on the same number of cores for the same system size would be approximately ten times slower. In turn, gradient fields are calculated on each element separately with an exponentially fast convergence.

2.3. Existing resolution criteria for direct numerical simulations

The first estimation of spatial resolution requirements for direct numerical simulations of RBC were made by Grötzbach [16]. His criteria for confined convection cells consisted of (i) resolving the steep gradients in the velocity and temperature near the walls with a sufficient vertical grid width distribution and (ii) resolving the smallest relevant turbulence elements with a sufficiently small mean grid width. Based on tests of Nusselt number with a spectral code, Grötzbach's first criterion requires at least three nodes within the thermal boundary layer thickness for Prandtl numbers on the order of one or larger. For much smaller Prandtl numbers, more nodes may be necessary as the viscous boundary layer becomes much thinner than the thermal boundary layer. The second criterion translates to a relation between the mean grid width $\bar{\Delta}$ and the mean dissipation or diffusion scale. For $Pr \leqslant 1$ this relation is $\bar{\Delta} \leqslant \pi \langle \eta_K \rangle$ and for $Pr \geqslant 1$ it is $\bar{\Delta} \leqslant \pi \langle \eta_B \rangle$. Grötzbach then assumes that $\langle \eta_K \rangle$ and $\langle \eta_B \rangle$ can be approximated by

the mean kinetic energy dissipation rate $\langle\epsilon\rangle$ as in equation (3). By using an argument similar to equations (17) this leads to the following global criteria on the grid widths[4] :

$$\bar{\Delta} \leqslant \pi \left(\frac{Pr^2}{Ra(Nu-1)} \right)^{\frac{1}{4}} \quad \text{for } Pr \leqslant 1, \tag{25}$$

$$\bar{\Delta} \leqslant \pi \left(\frac{1}{Ra(Nu-1)} \right)^{\frac{1}{4}} \quad \text{for } Pr \geqslant 1. \tag{26}$$

The criteria of Grötzbach were revised by Stevens *et al* [31] based on DNS results using the second order FDM also used for comparison in this paper [33, 34]. They systematically found the Nusselt number to be overestimated in poorly resolved simulations, especially when the plume dynamics were not properly resolved. They suggested changing the *mean* grid width criteria to one that instead holds for the *largest* grid width in any spatial dimension, since the Kolmogorov length needs to always be resolved in order to properly characterize the flow. A similar perspective was developed in Bailon-Cuba *et al* [2]. Although Stevens *et al* [31] did not determine any exact resolution criteria, they did compute the volume averaged dissipation rates $\langle\epsilon\rangle$ and $\langle\epsilon_T\rangle$ and compared these values to the globally computed Nusselt number as we have done in equation (17). They found that for high enough Rayleigh number ($\geqslant 10^9$), even though the Grötzbach criteria was technically followed, and equation (17) was well-satisfied for the viscous dissipation rate, equation (17) was not as well-satisfied for the thermal dissipation rate.

A further revision was conducted by Shishkina *et al* [27], who used the Prandtl–Blasius theory to derive a lower bound on the number of nodes required to be placed in both the thermal and the viscous boundary layers such that the estimated Kolmogorov lengths in the boundary layers are adequately resolved. For higher Rayleigh number, this minimum bound is much larger than that suggested by Grötzbach. For example, for our parameter range ($Pr = 0.7$), Shishkina *et al* suggest a minimum of five nodes for $Ra = 2 \times 10^7$ but increasing to nine nodes for $Ra = 2 \times 10^9$.

We will also discuss our own results in light of these criteria, including Grötzbach and the revisions by Stevens and Shishkina. However, we will take this analysis one step further by investigating the implications of resolving not only the global but also the local dissipation scales.

2.4. Statistical properties for resolutions with different polynomial orders

In correspondence with the so-called h-type and p-type SEM, two routes of modification of the resolution exist. In the h-type SEM the number of primary elements, N_e, is varied, in the p-type SEM one changes the polynomial degree N of the basis functions on each element and keeps the number of elements fixed. In the following, we summarize efforts in both directions in order to study resolution effects for the gradient fields. Since the grid is non-uniform in all three directions the side lengths of an element are functions of the three coordinates, i.e. $\Delta x_e(x, y, z)$,

[4] The factor of π can be rationalized to our view by the resolution criteria as formulated for pseudospectral box turbulence simulations (see e.g. [22]). There, $k_{max}\langle\eta_K\rangle \geqslant 1$ should be satisfied with the maximum resolved wave number (after de-aliasing) $k_{max} = \sqrt{2}N_x/3$ and $N_x = N_y = N_z$ equals the number of grid points in each direction. The standard box length is then the periodicity length of the Fourier modes $L_x = 2\pi$ and thus $N_x = 2\pi/\bar{\Delta}$.

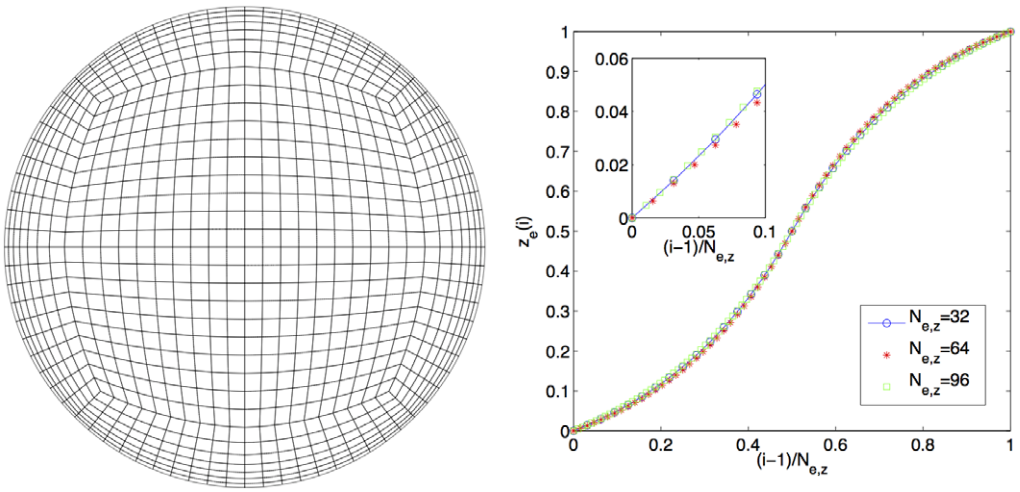

Figure 1. Left: display of the horizontal primary node structure as used for runs SEM1 to SEM4 displayed in table 1. Right: display of the vertical primary node mesh for runs SEM5 to SEM10 (see table 2). The stretching factors r are $r = 0.91$ for $N_{e,z} = 32$, $r = 0.95$ for $N_{e,z} = 64$ and $r = 0.97$ for $N_{e,z} = 96$.

$\Delta y_e(x, y, z)$ and $\Delta z_e(x, y, z)$. Figure 1 (left) shows a view of the horizontal primary element mesh. The coarsest elements are always found at the cell center line.

Particular emphasis was given here to the vertical resolution since this is the important direction for the correct resolution of the boundary layers. The formula that has been chosen to determine the element boundaries in the vertical direction is given by the following geometric scaling for the upper half of the cell with the scaling factor r:

$$\Delta z_e\left(\frac{N_{e,z}}{2}\right) + \cdots + \Delta z_e(1) = \left(\sum_{k=1}^{\frac{N_{e,z}}{2}} r^{k-1}\right) \Delta z_e(1) = \frac{1}{2}. \tag{27}$$

In correspondence with the up–down-symmetry this relation has to be applied for the lower half as well. Equidistant vertical meshing corresponds to $r = 1$. Figure 1 (right) demonstrates the resulting vertical meshing for different numbers of primary element nodes, $N_{e,z}$. In the appendix, we describe one way to obtain an optimal non-equidistant grid with respect to z, in other words, an optimal scaling factor r in (27).

Figure 2 shows important statistical quantities for a variation in correspondence with a p-type refinement. Results are obtained for different polynomial orders but the same primary element mesh. The results are summarized in table 1. In all cases shown, derivative-based quantities are evaluated spectrally on each element and no derivatives are taken across boundaries. All runs are conducted at a Rayleigh number $Ra = 10^8$ with a primary element mesh as displayed in figure 1. On average, we ran our simulations for at least 30 free-fall times T_f to ensure that the system had settled into its relaxed state, and then we continued the evolution for at least 75 free-fall times (in case of the biggest DNS), outputting on average at least 80 statistically independent snapshots.

Both the table and the figure indicate that insufficient spectral resolution is manifested in multiple ways, but is not necessarily obvious when looking at standard quantities, e.g. the

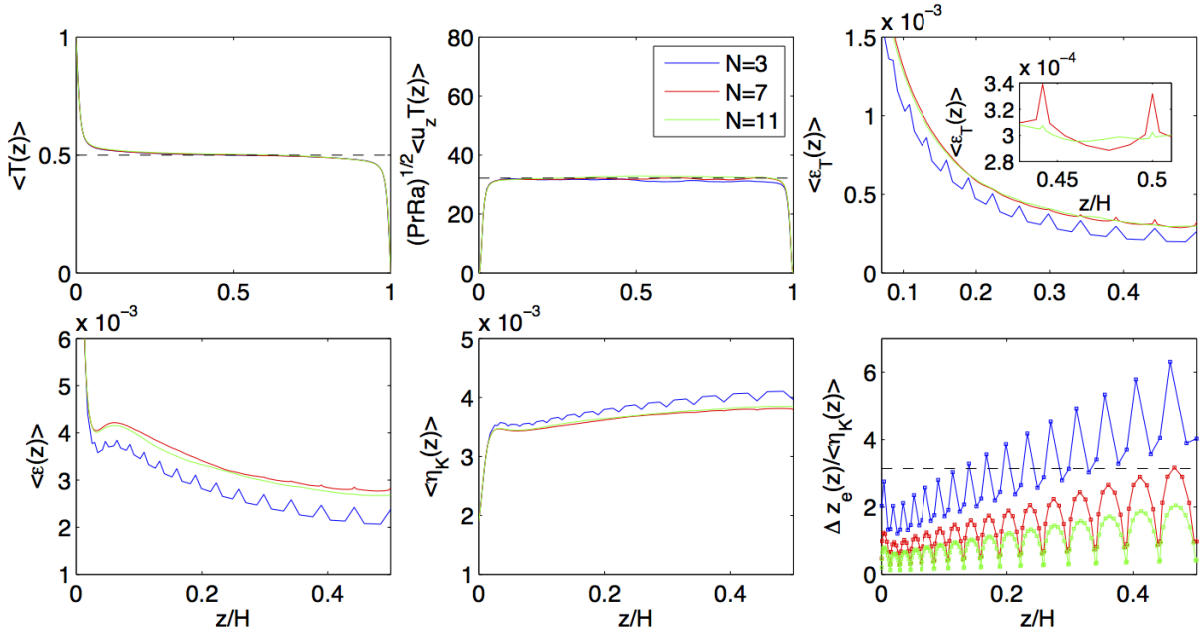

Figure 2. Resolution tests for $Ra = 10^8$ and $N = 3, 7$ and 11 using the same primary mesh (runs SEM1, SEM3 and SEM4 in table 1). We compare the mean temperature profile $\langle T(z)\rangle_{A,t}$, the mean convective flux profile $\sqrt{Ra\ Pr}\langle u_z T\rangle_{A,t}$, vertical profiles of mean thermal dissipation $\langle \epsilon_T(z)\rangle_{A,t}$ and mean kinetic energy dissipation $\langle \epsilon(z)\rangle_{A,t}$, a z-dependent Kolmogorov scale $\langle \eta_K(z)\rangle_{A,t}$ and how well the Grötzbach criterion is satisfied plane by plane $\Delta z_e(z)/\langle \eta_K(z)\rangle_{A,t}$. The dashed line in the lower right panel marks $\Delta z_e(z)/\langle \eta_K(z)\rangle_{A,t} = \pi$. The dashed line in the upper mid panel is the Nusselt number from run FDM3 (see table 2 or [2]). The inset in the top right panel magnifies the vertical profile of the mean thermal dissipation rate.

ingredients for the turbulent heat flux. The graphs for the mean temperature profile $\langle T(z)\rangle_{A,t}$, the convective heat flux $\sqrt{Ra\ Pr}\langle u_z T\rangle_{A,t}$ and even the Nusselt numbers which are obtained in different ways do not indicate a resolution effect at first glance. However the large magnitude of the relative errors of run SEM1 which has been used to test the dimensionless energy balances (19) is definitely caused by the insufficient resolution. The run SEM1 was one of our longest, taking about 1200 T_f. The statistical analysis is based on 192 turbulence statistically independent three-dimensional snapshots separated by six free-fall times each.

An increase to $N = 5$ in run SEM2 improves the convergence of the energy balances drastically. Nevertheless, the plane-averaged mean profiles of the thermal and the kinetic energy dissipation rates still display an insufficient resolution which is present for the next higher polynomial order, $N = 7$, as well. This becomes visible by the discontinuities at the element boundaries, especially near the center of the cell. The lower right panel of figure 2 relates a refined Kolmogorov-type scale

$$\langle \eta_K(z)\rangle_{A,t} = \frac{Pr^{3/8}}{Ra^{3/8}}\langle \epsilon(z)\rangle_{A,t}^{-1/4}. \tag{28}$$

Table 1. Parameters of the different spectral element simulations SEM1 to SEM4. The runs have an identical primary node mesh, but different polynomial order on each element. We display the order N of the Legendre polynomials, the total number of spectral elements, N_e, the number of spectral elements with respect to z direction, $N_{e,z}$, the number of grid cells resulting from primary and secondary nodes with respect to z direction, $N_z = N_{e,z}N$, and the Nusselt numbers $Nu(z=0)$, $Nu(z=1)$ and Nu_V. Furthermore we list the relative errors Λ_T and Λ_v (see equations (19)). All four runs are at $Ra = 10^8$, $\Gamma = 1$ and $Pr = 0.7$.

Run	N	$(N_e, N_{e,z})$	N_z	$Nu(0) \pm \sigma$	$Nu(1) \pm \sigma$	$Nu_V \pm \sigma$	Λ_T	Λ_v
SEM1	3	(30720, 32)	96	33.2 ± 0.9	33.2 ± 0.9	31.5 ± 2.1	5.6%	13.6%
SEM2	5	(30720, 32)	160	31.5 ± 0.7	31.7 ± 0.7	31.8 ± 2.1	0.3%	0.6%
SEM3	7	(30720, 32)	224	31.8 ± 0.9	31.9 ± 0.9	32.0 ± 3.1	0.3%	0.1%
SEM4	11	(30720, 32)	352	31.6 ± 0.6	31.9 ± 0.6	31.8 ± 2.0	0.1%	0.5%

We can refine the classical Grötzbach criterion (25) to

$$\frac{\Delta z(z)}{\langle \eta_K(z) \rangle_{A,t}} \leqslant \pi, \tag{29}$$

where Δz is the vertical grid spacing, recognizing now element mesh and collocation grid on each element. This is exactly what produces the characteristic shape of all the curves in the lower right panel. Such a criterion has been suggested already by Bailon-Cuba *et al* [2]. It shows clearly that all orders $N \leqslant 7$ result in grid spacings that are too coarse in the bulk region of the convection cell. In the appendix, we demonstrate how insufficient resolution can cause the spike structures in the vertical profiles of the dissipation rates and related quantities by means of a convergence test for a simple analytical profile. The artifacts at the element boundaries which we see for the SEM are due to insufficient resolution and hence the failure of the derivatives to match at the boundaries, since this SEM method enforces only the continuity of the functions at the boundaries. This gives rise to a clear criterion for resolution: when the system is sufficiently resolved, all spikes in both dissipation profiles completely disappear. In classical FDMs numerical diffusion and dispersion will suppress such spikes. In addition it is shown in the appendix that similar observations as in figure 2 follow when the h-type route of grid refinement is followed, i.e. refining the primary mesh at fixed system parameters (Ra, Pr, Γ) and a given polynomial order. To conclude this part, while some standard indicators for sufficient resolution which have been discussed in previous works [27, 31] are all well-satisfied, a closer look at the dissipation fields indicates clearly that the spatial resolution is not sufficient, in particular in the bulk of the cell. The artifacts in the mean vertical profiles of the gradient fields do not completely disappear even when the order is increased to $N = 11$ as demonstrated in the inset in the top right panel of figure 2.

Compared to previous resolution studies of fluid turbulence in periodic boxes [23] and shear flow turbulence channels [14], the situation in the present RB case is more complex. On the one hand, the turbulent flow is inhomogeneous in all space dimensions. This causes space-dependent statistical properties of the turbulent fields and their derivatives. On the other hand, the computational grid is non-uniform in all three directions as described already above.

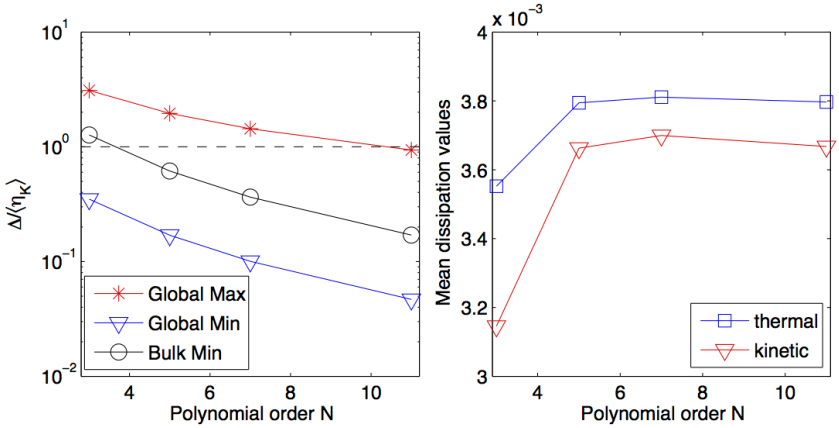

Figure 3. Left: global maximum and minimum grid spacing as well as minimum grid spacing in the bulk region (volume V_b) for the data in table 1. Data are normalized with respect to mean Kolmogorov length. The definitions are given in (30) and (31). Right: mean dissipation rates of thermal variance, $\langle \epsilon_T \rangle_{V,t}$, and kinetic energy, $\langle \epsilon \rangle_{V,t}$, as functions of the polynomial order.

Although we refine the grid toward all walls, the regions where one expects the largest amplitude of the derivatives, it is not necessarily assured that both, steepest gradient and finest grid cells, coincide. In this situation one can however define the coarsest and finest grid spacing in the whole cell or a subvolume to get a global indication of the quality of resolution. This is done by the following geometric means:

$$\Delta_\mathrm{max} = \sqrt[3]{\max_{x\in\mathcal{I}} \Delta x_\mathrm{e}(x,y,z) \max_{y\in\mathcal{I}} \Delta y_\mathrm{e}(x,y,z) \max_{z\in\mathcal{I}_z} \Delta z_\mathrm{e}(x,y,z)}, \tag{30}$$

$$\Delta_\mathrm{min} = \sqrt[3]{\min_{x\in\mathcal{I}} \Delta x_\mathrm{e}(x,y,z) \min_{y\in\mathcal{I}} \Delta y_\mathrm{e}(x,y,z) \min_{z\in\mathcal{I}_z} \Delta z_\mathrm{e}(x,y,z)} \tag{31}$$

with $\mathcal{I} = [-0.5, 0.5]$ or a subinterval and $\mathcal{I}_z = [0, 1]$ or a subinterval, such as the bulk volume V_b which is given further below in the text. In figure 3 (left) we display the minimum and maximum grid spacing for the whole cell obtained by (30) and (31). Furthermore, we show the minimum resolution in the bulk region where we defined a subvolume $V_\mathrm{b} = \{\mathbf{x} = (r, \phi, z) | \, 0 \leqslant r \leqslant 0.3; \, 0.2 \leqslant z \leqslant 0.8\}$. The right panel confirms what we have discussed already above, that the mean dissipation rates level off for $N \geqslant 5$ although vertical profiles are still not sufficiently well resolved.

In figure 4 we display the probability density functions (PDFs) of the fields ϵ_T and ϵ. The upper row shows data which have been obtained in the whole cell, the lower row those for the subvolume V_b in the bulk. It can be seen for all four panels that with increasing polynomial order more very-high-amplitude events are resolved and that the tail is further stretched out. The better resolution manifests in significantly less scatter at the largest amplitudes. Even more pronounced are the resolution effects in the bulk (lower row). We observe now for both dissipation rates the same systematic trend. The tail of the stretched exponential distribution is fatter for higher polynomial order. This latter finding is also in agreement with previously reported spectral resolution studies for homogeneous isotropic box turbulence as reported in [23]. Note that the tails of the exponents in our figure do not always increase in an even manner with resolution.

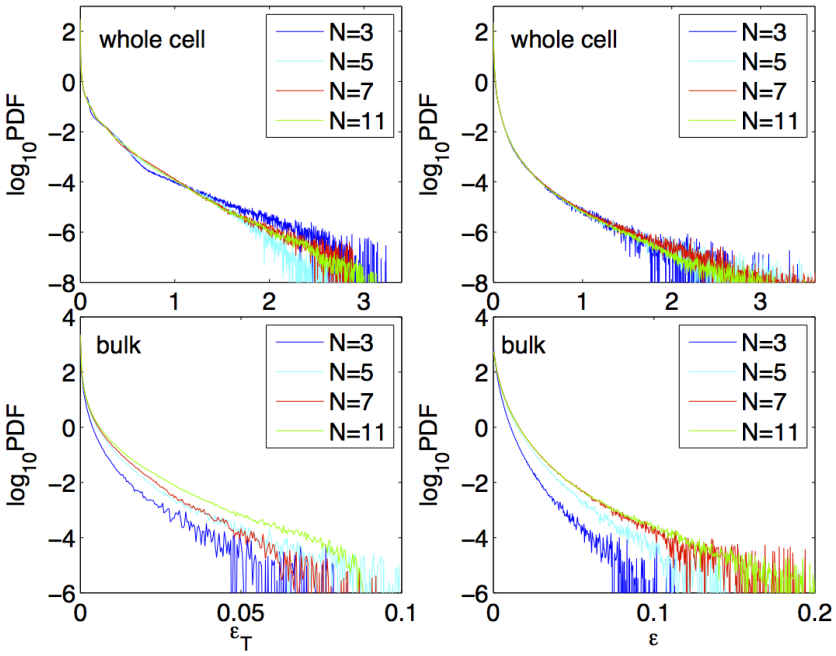

Figure 4. PDFs of the thermal dissipation rate (left column) and kinetic energy dissipation rate (right column) are shown for runs SEM1 to SEM4. The upper row displays the data obtained for the whole cell. The lower row shows the data for the bulk.

One sees for example, a jump in the lower left panel of figure 4 in going from $N = 3$ to 5 and then again from $N = 7$ to 11. This is understandable in light of figure 12, where we see that high-amplitude events can increase the tails significantly. Since the system is chaotic as well as turbulent, simulations done for the same Rayleigh number but different resolution are statistically different, so some of them could have more high amplitude events than others. Longer simulation times would help smooth this out.

2.5. *Comparison with the finite difference method*

The comparison of DNS runs at $Ra = 10^9$ and $Pr = 0.7$, i.e. runs SEM9, SEM10 and FDM1 from table 2, is displayed in figure 5. The resolution of FDM1 has been chosen twice as fine as in the run from Bailon-Cuba *et al* [2] in order to get a comparable number of grid points with respect to SEM9. The thermal boundary layer for FDM1 is resolved with 21 grid planes. We see that the agreement of the mean vertical profiles is very good. The value of the Nusselt numbers for the higher resolution runs match now to within three significant figures, also with the data from [35]. In table 2, we list also the corresponding relative errors Λ_T and Λ_v which are larger for FDM1 than those for SEM9 and SEM10, particularly for the kinetic energy dissipation rate in our study. The latter has been evaluated in correspondence with (13) which has to be applied for inhomogeneous flows. The difference is supported by the deviation in the vertical profiles of $\langle \epsilon(z) \rangle_{A,t}$ in the lower left panel of figure 5. We also note that Stevens *et al* (see their table 1 in [31]) reported similar errors which were in their case however mostly detected for the thermal energy dissipation rate and not only for the lowest resolutions.

Table 2. Parameters of the different spectral element simulations. Runs SEM7, SEM8 and SEM10 have an order of the Legendre polynomials $N = 11$, runs SEM5, SEM6 and SEM9 use $N = 7$. We show the Rayleigh number Ra, the Prandtl number Pr, the total number of spectral elements, N_e, the number of spectral elements with respect to z direction, $N_{e,z}$, the number of grid planes (primary and secondary nodes) with respect to z direction, N_z, the total number of grid cells $N_e N^3$ and the Nusselt number Nu_V. Furthermore we list the relative errors Λ_T and Λ_v (see equation (19)). All simulations are conducted for $\Gamma = 1$ and $Pr = 0.7$. The finite difference run FDM1 is conducted for $N_\phi \times N_r \times N_z = 721 \times 361 \times 621$, respectively.

Run	Ra	Pr	N_e	$N_{e,z}$	N_z	$N_e N^3$	Nu_V	Λ_T (%)	Λ_v (%)
SEM5	10^6	0.7	30 720	32	224	1.05×10^7	8.6	0.1	0.1
SEM6	5×10^6	0.7	30 720	32	224	1.05×10^7	13.9	0.3	0.5
SEM7	10^7	0.7	30 720	32	352	4.08×10^7	16.6	0.3	0.6
SEM7a	10^7	6.0	30 720	32	352	4.08×10^7	16.6	0.7	0.2
SEM8	10^8	0.7	256 000	64	704	3.41×10^8	31.4	0.4	0.2
SEM9	10^9	0.7	875 520	96	672	3.00×10^8	62.8	0.1	0.1
SEM10	10^9	0.7	875 520	96	1056	1.17×10^9	63.1	1.2	0.5
FDM1	10^9	0.7	–	–	621	1.62×10^8	63.1	1.7	9.2

The distribution of the local amplitudes of both dissipation fields is compared in figure 6. Both panels show that the deviations arise mostly for the outer tails where the extreme fluctuations are captured. In case of the thermal dissipation rate both PDFs remain closely together for nearly the whole range. The kinetic energy dissipation rate data start to differ for roughly 15–20% of the maximum amplitude which might be one reason for the larger values of Λ_v. The agreement in the low-amplitude part of the PDFs is good as shown in both insets.

Furthermore, we find excellent agreement between the two codes when comparing global transport properties. For example, the Nusselt number and the globally averaged thermal dissipation rates for both the whole cell and the bulk volume V_b as shown in figure 7 agree quite well. We varied our Rayleigh number between 10^6 and 10^9 and compared with fits of the FDM data from [2, 7, 8], respectively. We did need to use a different prefactor for the bulk-averaged thermal dissipation rate since our subvolume V_b was chosen differently.

To estimate the effect of the size of our subvolume on the thermal dissipation rates, we show two additional data sets in the right panel of figure 7: one for a smaller subvolume $8V_b/27$ and the other for an even smaller subvolume of $V_b/27$ (all centered about the middle of the cell). The general trend is for the thermal dissipation rates to slightly decrease as the subvolume decreases. Also, our uncertainty becomes larger as the subvolume decreases. We estimated the uncertainty in the mean $\langle \epsilon_T \rangle_{V,t}$ values by computing the difference between the mean taken over the entire time series and the mean taken over only the latter half of the time series.

The fits to the data sets corresponding to the smallest subvolumes are $\langle \epsilon_T \rangle_{8V_b/27,t} = (0.21 \pm 0.07) Ra^{-0.40 \pm 0.02}$ and $\langle \epsilon_T \rangle_{V_b/27,t} = (0.25 \pm 0.12) Ra^{-0.42 \pm 0.03}$. Kaczorowski and Xia [17] also studied the scaling of subvolume-averaged thermal dissipation rates in a similar range of Rayleigh numbers using a small subvolume ($V/64$) but for a Prandtl number of 4.38. Our exponent disagrees with theirs of $\langle \epsilon_T \rangle_{V,t} = 43.9 Ra^{-0.78}$. We do see a trend toward a larger

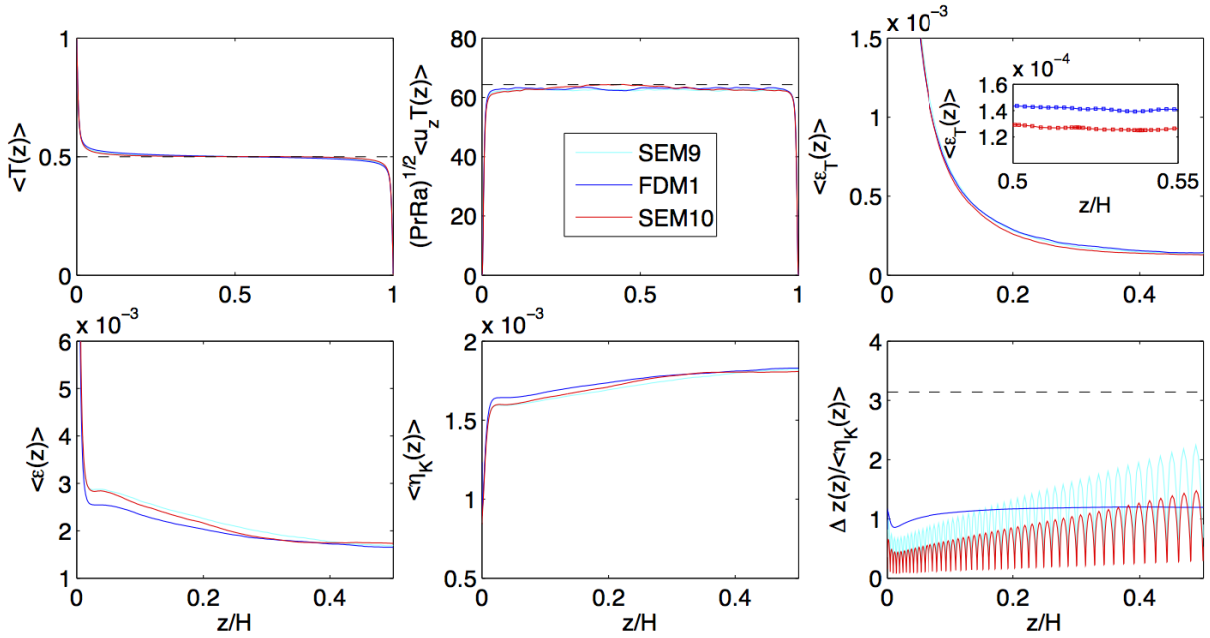

Figure 5. Comparison of spectral element runs SEM9 and SEM10 with finite difference run FDM1 (see table 2 for specifications). The same quantities are plotted as in figure 2. The dashed line in the lower right panel marks $\Delta z(z)/\langle \eta_K(z)\rangle_{A,t} = \pi$. The dashed line in the upper mid panel is the Nusselt number of the FDM run from [2]) with $Nu = 64.3$. The inset in the top right panel magnifies the thermal dissipation rate profiles for FDM1 and SEM10.

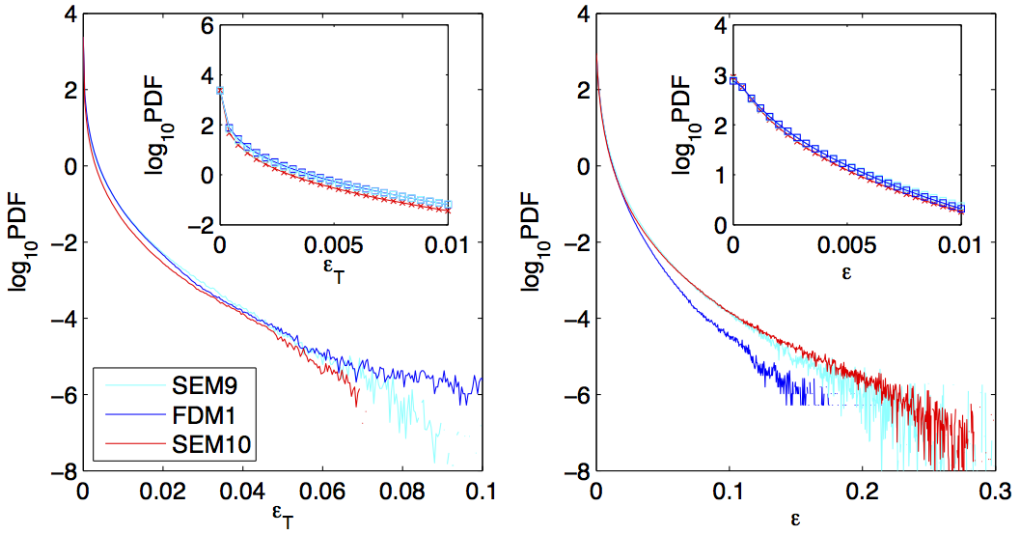

Figure 6. Comparison of the PDFs of ϵ_T (left) and ϵ (right) obtained in the subvolume V_b. The insets magnify the smaller amplitudes. We compare the data for FDM1 with those from SEM9 and SEM10. Line colors are the same for both figures and indicated in the legend and agree with those from figure 5.

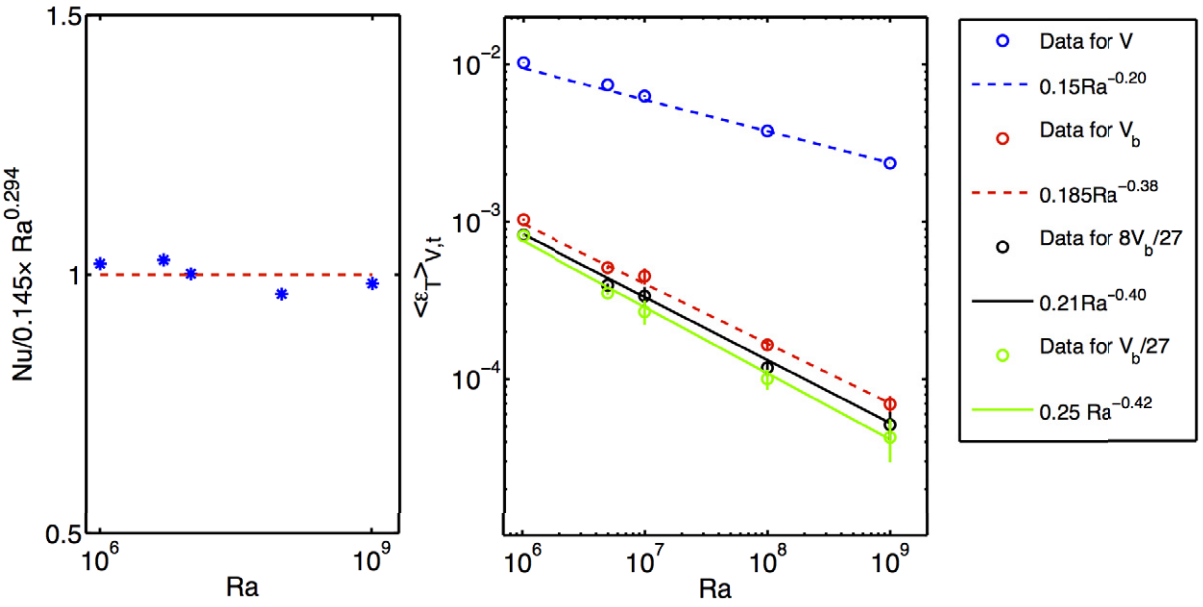

Figure 7. Comparison of global transport properties between SEM and FDM. Left: Nusselt versus Rayleigh number for $10^6 < Ra < 10^9$. The data are compensated by the power law $Nu = 0.145 \times Ra^{0.294}$ which was a fit to the data as reported in Bailon-Cuba *et al* [2]. Right: mean thermal dissipation as a function of the Rayleigh number for different subvolumes. The first two data sets are compared with fits to the FDM data (shown as dashed lines). For the whole cell V we take former results from [8], for the bulk volume V_b we compare with data from [7]. In this case the prefactor is different since the subvolume V_b was chosen differently. The last two series are obtained in smaller subvolumes and are fitted by power laws as given in the legend and shown as solid lines.

exponent as our subvolume decreases, but our largest exponent still disagrees with [17] even when including our estimates of numerical uncertainty.

3. Results

3.1. Very-high-resolution runs at different Rayleigh numbers

In the following section, we want to discuss a series of very-high-resolution runs in more detail. All the runs with their resolution are displayed in table 2. We first compare runs at $Pr = 0.7$ spanning a Rayleigh number range from 10^7 to 10^9.

Snapshots of high-amplitude regions of both dissipation fields are shown in figure 8. The data are given in logarithmic units. Both dissipation rates form smooth sheet-like structures in the bulk, in particular the thermal dissipation rate. The very fine resolution is clearly obvious from the absence of ripples at the isosurfaces of both dissipation fields. In figure 9 we show horizontal slices of both dissipation fields at fixed height z. Again the data is given in logarithmic units to highlight the variation. The top row is for $\epsilon_T(x, y)$ and the bottom corresponds to $\epsilon(x, y)$. The left column is for the bottom plate, $z = 0$, and the right column is for the midplane,

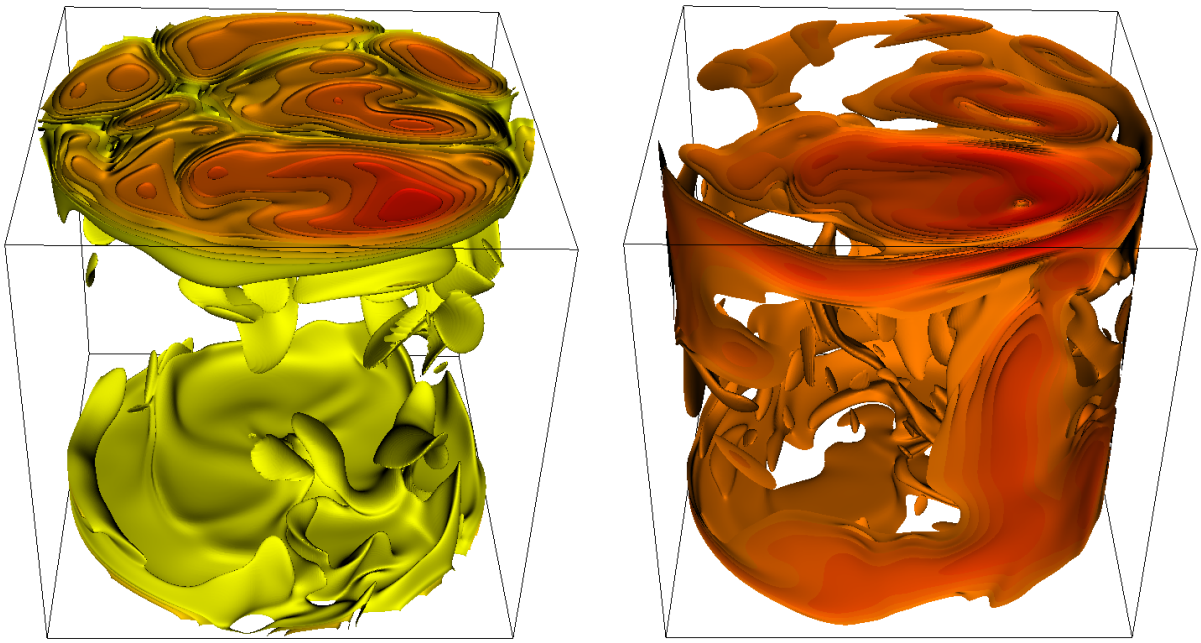

Figure 8. Isovolume plots for the thermal dissipation rate (left) and the kinetic energy dissipation rate (right). Data are obtained for $Ra = 10^7$, $Pr = 0.7$ and are shown in logarithmic units. Left: the range of the data is $\log(\epsilon_T) \in [-21.1, 0.5]$ and isosurfaces between -5 and 0 are shown. Right: the range of the data is $\log(\epsilon) \in [-37, 0.0]$ and isosurfaces between -4.5 and 0 are shown. Data are from SEM7 in table 2.

$z = 0.5$. We see a smaller range of scales at midplane than near the bottom plate, consistent with figure 4. The fine filamentary structure present in this case is similar to passive scalar turbulence [37] or convectively driven mixing layers [18]. Interestingly the thermal dissipation rate appears to be correlated with the kinetic dissipation rate at the bottom plate, but less so at the midplane. At the bottom plate the structures reflect the ongoing plume formation and detachment.

The distribution of the locally fluctuating dissipation scales $\eta_K(\mathbf{x})$ as defined in (5) is shown figure 10 for runs SEM7, SEM8 and SEM10. The scales have been analyzed in the whole cell with volume V as well as in a bulk region which is defined by V_b. The definition (5) has been chosen for this analysis which can be straightforwardly applied to the non-uniform grids that have been used for all DNS. An alternative definition of local dissipation scales which is based on velocity increments was suggested in [38, 39]. In [14], it was shown how both distributions can be related to each other. It can be observed first that the scales in the whole cell cover a wider range, both, to the large- and small-scale end (see top left panel) which is centered around the most probable value which is always close to mean dissipation scale $\langle \eta_K \rangle_{V,t}$ which is calculated following (18). This finding is also in agreement with previous DNS results [7, 8] which show that dissipation rates have significantly higher amplitudes in the boundary layers. We also see that the right tail ends of the distributions in the whole cell decrease with Rayleigh number. It demonstrates that the scales in turbulent RBC become finer as the Rayleigh number increases. This argument is also supported by the fact that the differences

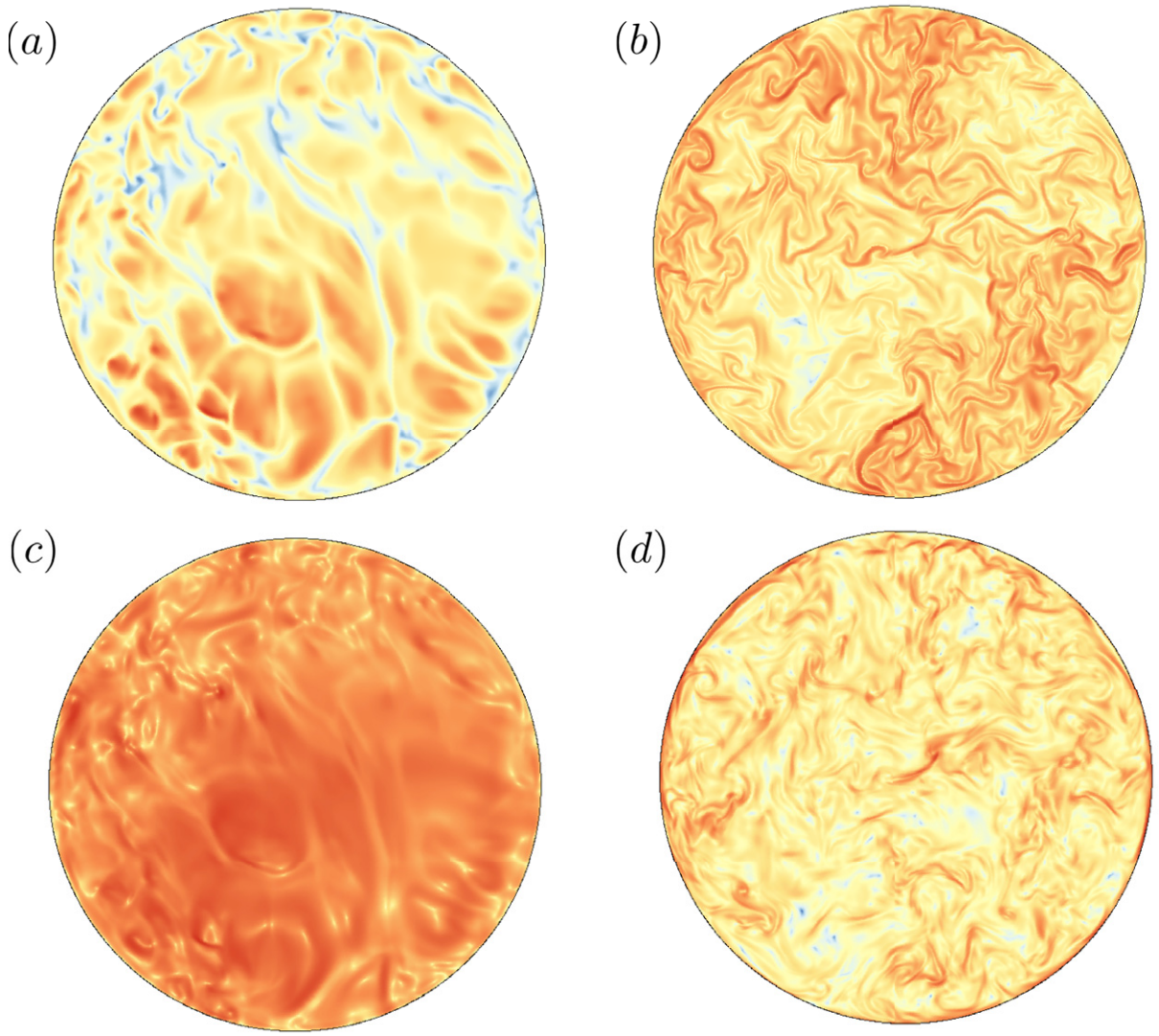

Figure 9. Snapshots of the local thermal dissipation rate $\epsilon_T(x, y)$ for (a) $z = 0$ and (b) $z = 0.5$ and the local kinetic energy dissipation rate $\epsilon(x, y)$ also for (c) $z = 0$ and (d) $z = 0.5$. Data are obtained for $Ra = 10^9$, $\Gamma = 1.0$ and $Pr = 0.7$ and are shown in logarithmic units. Data are from SEM10 in table 2. The range of the data is $\log(\epsilon_T) \in$ (a) $[-2.8, 0.3]$, (b) $[-11.0, -2.0]$ and $\log(\epsilon) \in$ (c) $[-10.0, 0.0]$, (d) $[-6.0, -1.2]$.

between the distributions in V and V_b become smaller. In the top right figure, we zoom into the left tail end for all six data sets. The smallest local dissipation scales are associated with the largest dissipation events which arise for very steep local gradients. With increasing Rayleigh number these contributions become larger, i.e. the left tail becomes fatter. A similar behavior, however much less pronounced, can be observed if one restricts the analysis to the bulk volume V_b. In figure 11, we display the PDFs of both dissipation rates in the whole cell and in the bulk. For both rates, it can be clearly seen that the major contribution to the high-amplitude events comes from the boundary layer regions. This has been studied already in [7].

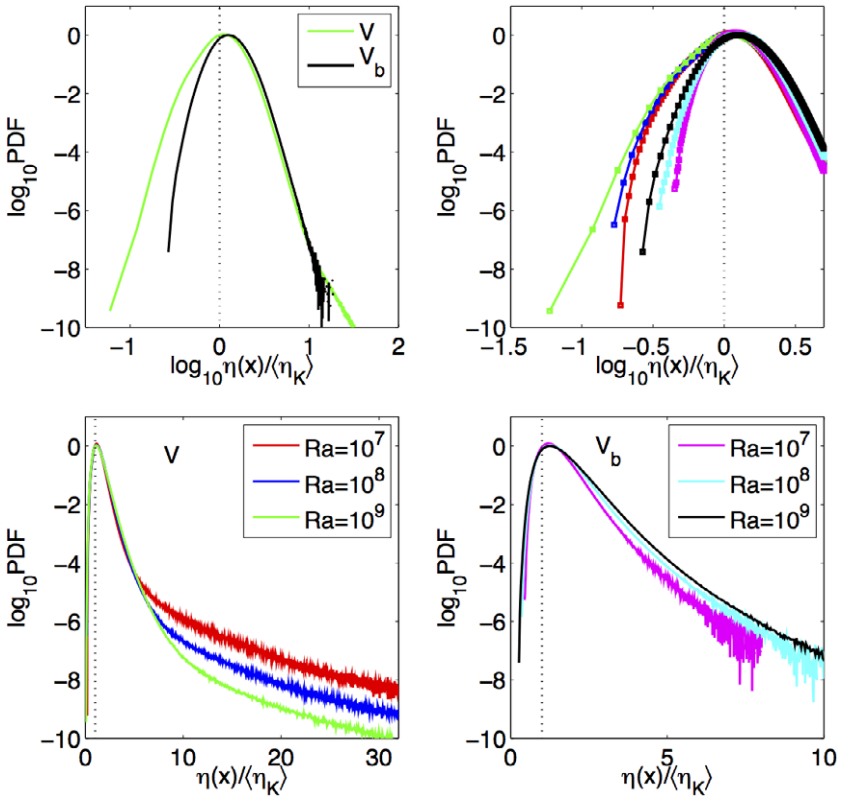

Figure 10. PDF of the local dissipation scale $\eta(\mathbf{x}, t)$ for runs SEM7, SEM8 and SEM10 as given in the legend and table 2. We compare the PDFs obtained in the whole convection cell with volume V and those obtained in the bulk which is defined as the subvolume V_b. The dotted lines indicate $\eta = \langle\eta_\mathrm{K}\rangle$. Top left: comparison of the PDFs in V and V_b for $Ra = 10^9$. Top right: magnification of the left tails for all six data sets. Bottom left: Rayleigh number dependence in the whole cell. Bottom right: Rayleigh number dependence in the bulk. Line colors are uniquely chosen for all plots and indicated in the legends.

Figure 12 illustrates the sensitivity of the statistics with respect to a single extreme event that was monitored in the course of the simulation run and can be identified as a large scale plume sweeping through the bulk volume. It causes a large instantaneous thermal dissipation which is not easily detectable in the mean dissipation $\langle\epsilon_T(t)\rangle_{V_\mathrm{b}}$. Only in the fourth moment of the thermal dissipation $\langle\epsilon_T^4\rangle$ which is taken in the bulk volume does this strong event become clearly visible as seen in the right panel of figure 12. Note also that the fourth moment in the whole cell is also fairly insensitive to this particular high-amplitude bulk event. The impact of this single event on the statistics is shown in the left panel of figure 12. As expected the tail is stretched significantly.

In figure 13 we display a time sequence of the dynamics which is associated with this single extreme event. The upper panel of the figure replots the moments of the thermal dissipation rate obtained in V_b with respect to time but on a finer time scale. It can be observed that the entire event lasts less than two free-fall times. We find that the fourth-order moment increases by

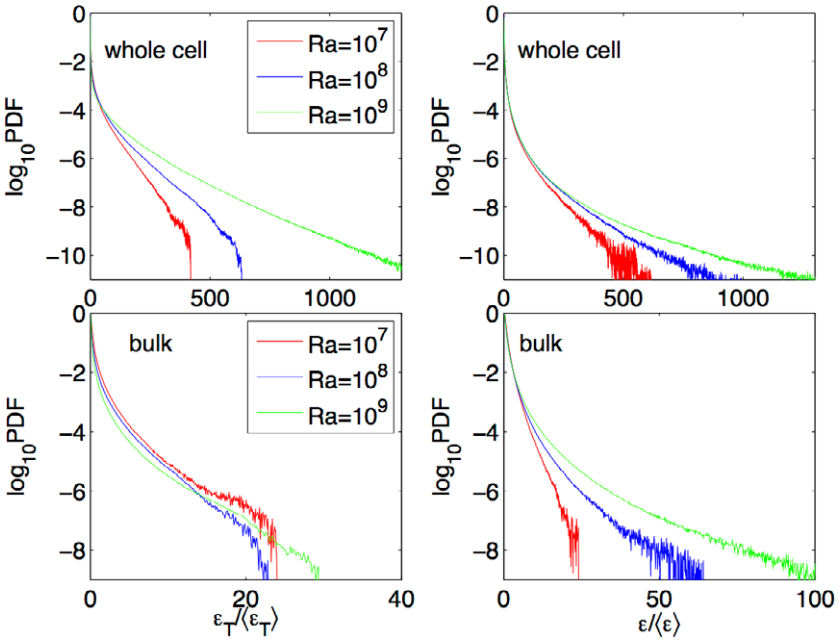

Figure 11. PDF of the dissipation rates for runs SEM7, SEM8 and SEM10 as given in the legend and table 2. We compare the PDFs obtained in the whole convection cell (upper panels) and those obtained in the bulk which is defined as the subvolume V_b (lower panels). Thermal dissipation rates are displayed in the left column, energy dissipation rates in the right one.

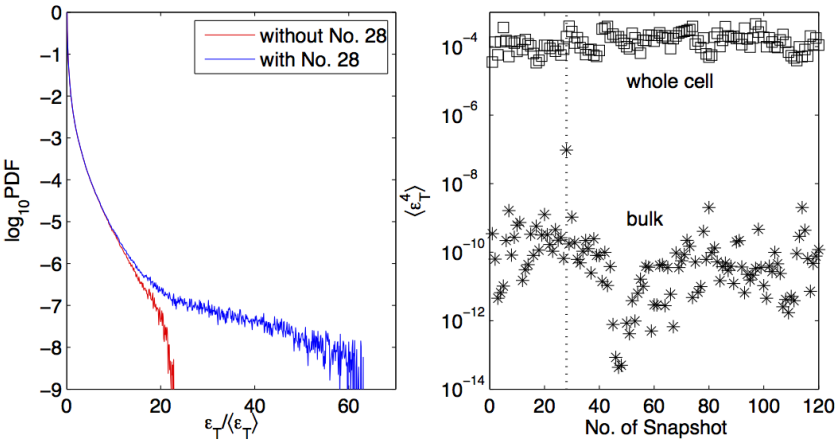

Figure 12. Impact of high-amplitude dissipation events on the tail of the PDF of the thermal dissipation rate for SEM8. Left: PDFs with and without the high-amplitude event (snapshot no. 28). Right: fourth-order dissipation rate moments in the whole cell and the bulk. The dashed line indicates snapshot no. 28.

about three orders of magnitude within this short period. Figures 12 and 13 clearly show that the statistical fingerprint of this strong event is best detected in the higher-order moments. The bottom panels of figure 13 show vertical slice images of the thermal dissipation rate and the

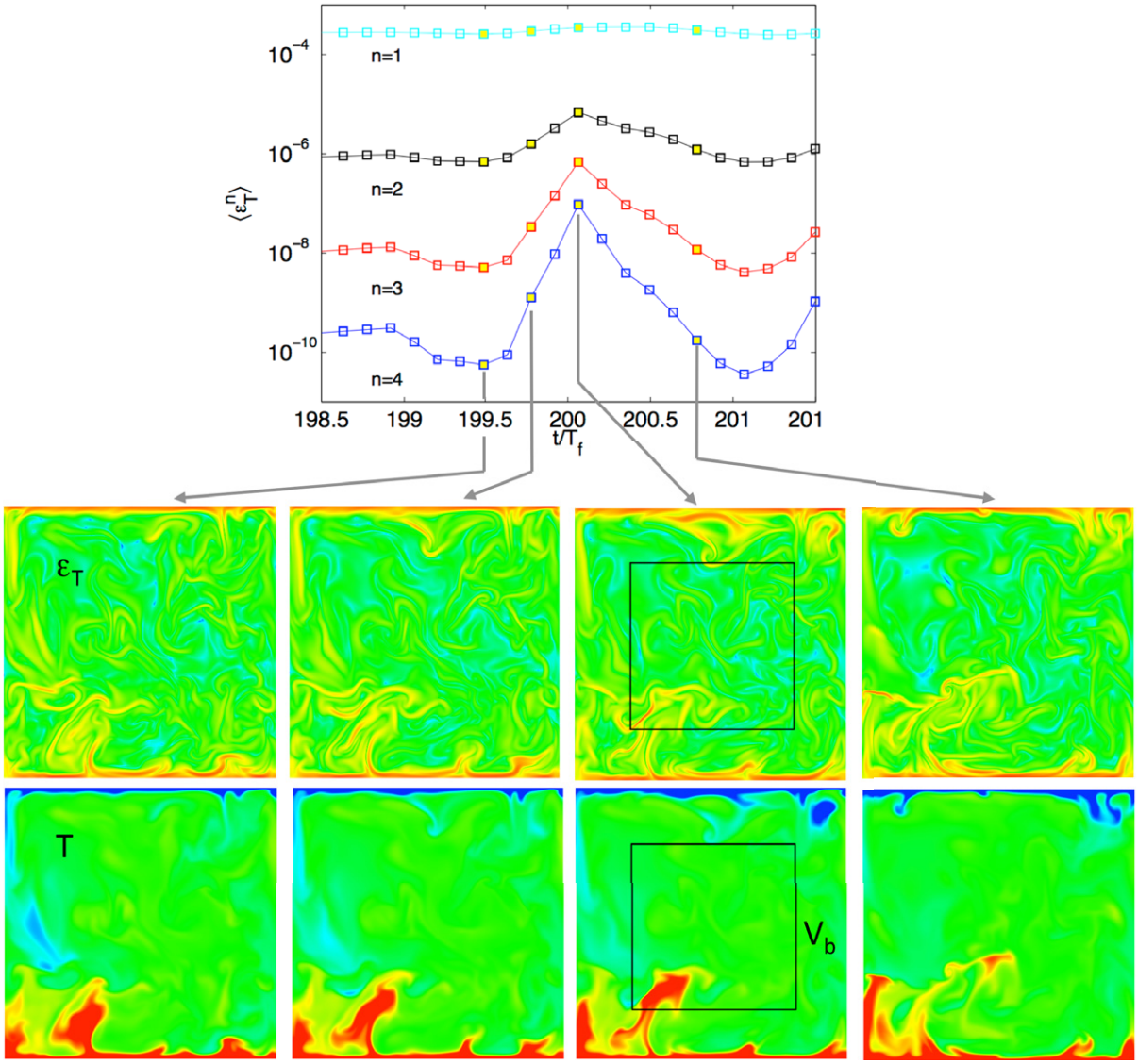

Figure 13. The dynamical sequence of the high-amplitude dissipation event from figure 12. The top panel displays the temporal evolution of the thermal dissipation rate moments of order $n = 1$–4 calculated in V_b. The times which correspond to the images have been plotted as symbols filled with yellow. The first row below the top panel displays vertical slice images of the logarithm of the thermal dissipation rate field taken in the plane $(x = 0, y, z)$. The range of the data is $\log(\epsilon_T) \in [-20, 0.1]$. The bottom row shows the corresponding temperature and the range of the data is $T \in [0.3, 0.7]$. We also highlight the size of the subvolume V_b in comparison to the full volume V. Data are obtained for run SEM8.

temperature corresponding to four different times in the evolution of this event. Clearly visible is the pronounced hot plume rising and then detaching from the bottom plate which generates steep temperature gradients and thus a large amplitude of the thermal dissipation rate.

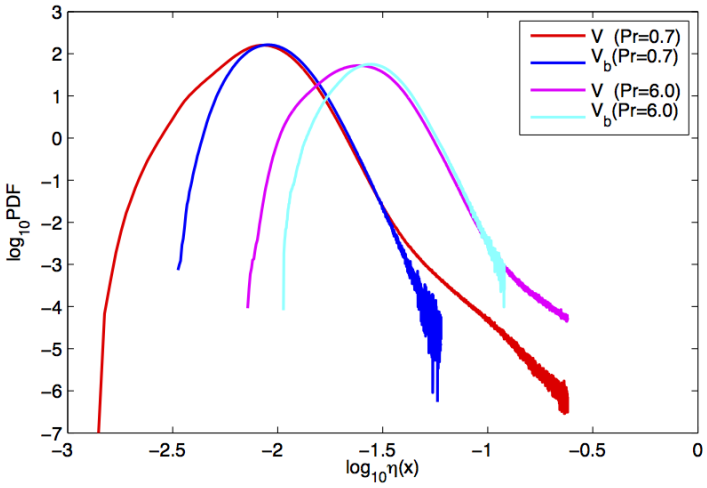

Figure 14. PDFs of the local dissipation scales obtained in the whole cell and the bulk subvolume for SEM7 and SEM7a.

3.2. Very-high-resolution run at higher Prandtl number

Lastly, we compare the gradient statistics at a given Rayleigh number for two different Prandtl numbers. Runs SEM7 and SEM7a are conducted at $Ra = 10^7$ and $Pr = 0.7$ (air) and 6 (water). The data in table 2 indicates already that the resolution requirements remain the same for the enhancement of the Prandtl number by a factor of nearly 10. For $Pr > 1$, the mean diffusion scale of the temperature field, $\langle \eta_B \rangle$ is smaller than mean Kolmogorov scale, $\langle \eta_K \rangle$, since a viscous-convective range on scales smaller than the Kolmogorov scale builds up. Figure 14 displays the distributions of $\eta_k(\mathbf{x}, t)$. We observe again that the range of varying scales is larger when the data are taken in the whole cell in comparison to the bulk volume.

We have not rescaled the distributions by the corresponding mean dissipation scale since we want to point to the shift of both PDFs for $Pr = 6$. This means that the local dissipation scales are larger as a whole than for the case of $Pr = 0.7$. This behavior looks counter-intuitive at first glance, particularly from the perspective of passive scalar mixing at increasing Prandtl (or Schmidt) number [22]. There one detects increasingly finer diffusion scales for the passive scalar leaving however the local dissipation scales unchanged. For turbulent convection, we estimated already in the introductory part that the relatively slow falloff of $\langle \eta_B \rangle \sim Pr^{-1/8}$ as we progress from $Pr \approx 1$ to $Pr \gg 1$. It is the active nature of the temperature field which causes this different behavior in the convection case as compared to passive mixing. A temperature field at a higher Prandtl number exists on finer scales than a velocity field, obeying narrower plume structures which causes a weaker driving of the fluid motion resulting in less steep velocity gradients and consequently larger local dissipation scales. This argumentation is also supported by a comparison of the PDFs of both dissipation fields as shown in figure 15. High-amplitude events and tails are shifted to smaller magnitudes in all cases.

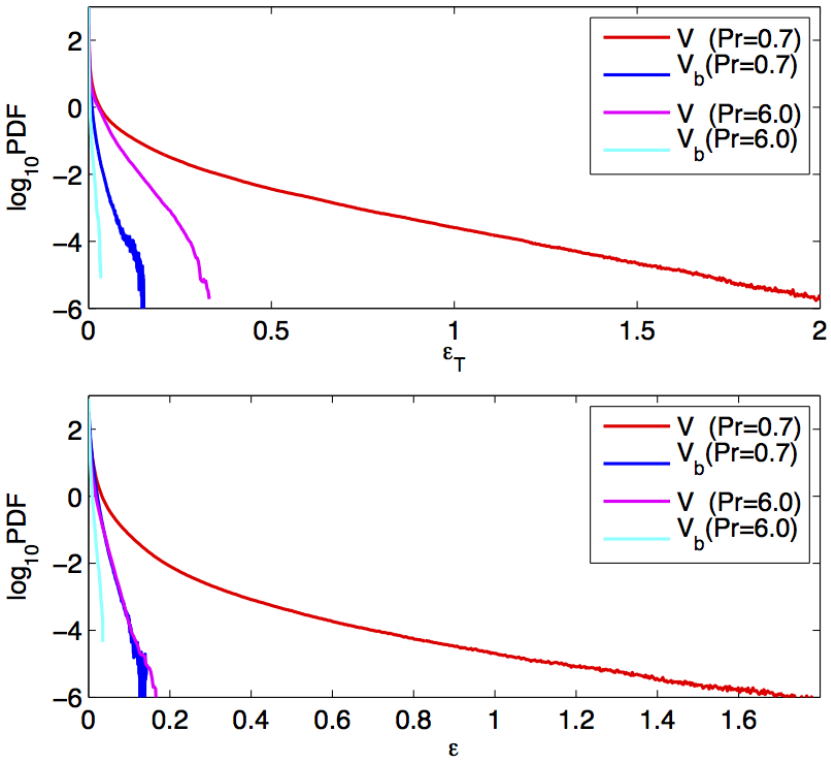

Figure 15. PDFs of the thermal dissipation (top) and kinetic energy dissipation rates (bottom), respectively. We compare runs SEM7 and SEM7a for the analysis in the bulk V_b and the whole cell V.

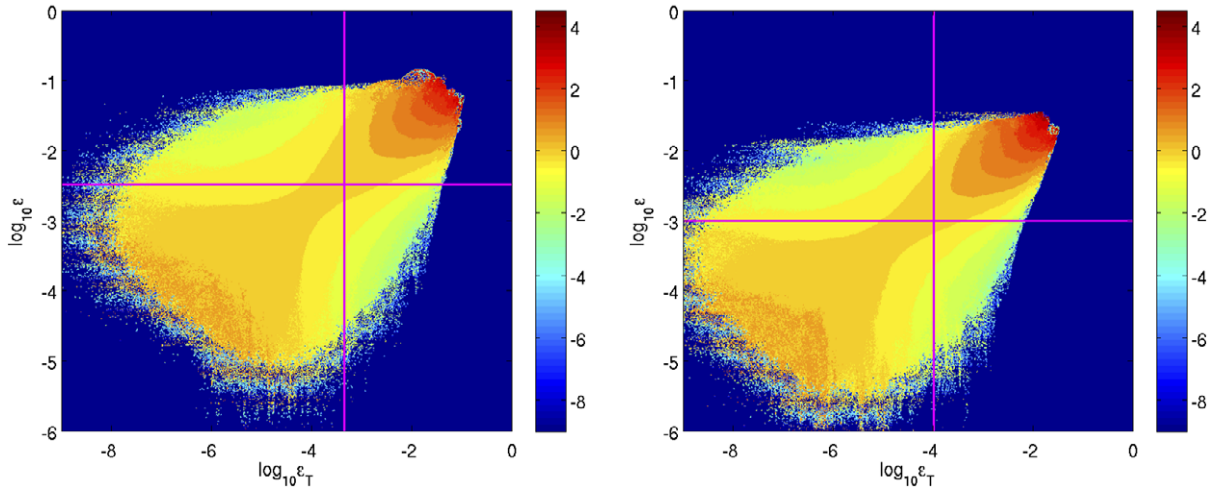

Figure 16. Joint statistics of both dissipation rates $\Pi(\epsilon_T, \epsilon)$ as given by (32) for SEM7 and SEM7a. Left: $Pr = 0.7$. Right: $Pr = 6$. The vertical and horizontal lines indicate the corresponding mean dissipation rates. Data are obtained in V_b. The color scale is given in decadic logarithm.

3.3. Joint statistics

The joint statistics of both dissipation rates is displayed in figure 16. We show the joint and normalized PDF which is given by

$$\Pi(\epsilon_T, \epsilon) = \frac{P(\epsilon_T, \epsilon)}{P(\epsilon_T)P(\epsilon)}. \tag{32}$$

The contour levels are plotted in logarithmic values as indicated by the color bar. Similar to [17] for RBC or to [15] for a channel flow, the support of Π has an ellipsoidal form with a tip at the joint high-amplitude events. The joint PDF $P(\epsilon_T, \epsilon)$ is here normalized by the corresponding single quantity PDFs, $P(\epsilon)$ and $P(\epsilon_T)$. In this way we highlight the correlations between both fields. If $\Pi(\epsilon_T, \epsilon)$ is larger than unity then the correlation is larger than if the two dissipation rate fields were statistically independent. It can be observed that the support of the joint PDF for $Pr = 6$ is shifted to smaller amplitudes in comparison to $Pr = 0.7$, which is in agreement with figure 15. In both cases, the high-amplitude events are correlated strongest, exceeding the corresponding mean amplitudes by at least two orders of magnitude.

4. Summary and discussion

We have computed both global and local measures of dissipation and heat transport from high resolution direct numerical simulations of turbulent RBC using a SEM. We find that the global measures of heat transport, such as Nusselt number, time-averaged temperature profiles and volume-averaged dissipation rates, are fairly insensitive to insufficient resolution, as long as the mean Kolmogorov length is resolved. However, if one computes instead plane-averaged or even more local dissipation rates, one finds that the Grötzbach criteria (or something even more stringent as in (33)) needs to be satisfied for every grid point in order to have the system properly resolved. The main effects of a poorly resolved simulation are that some of the largest dissipation (both thermal and viscous) scales in the system are not resolved, especially in the bulk where the computational grid is coarsest. Our investigations suggest that the refined SEM analysis which we conducted to study the statistics of dissipation fields require at least

$$\frac{\Delta z(z)}{\langle \eta_K(z) \rangle_{A,t}} \lesssim \frac{\pi}{2} \quad \text{for } Pr \gtrsim 1. \tag{33}$$

This follows e.g. from the data displayed in figure 4 for the largest Rayleigh number. It is clear that such a criterion can be applied *a posteriori* only. Recall also that the horizontal spacing was always finer in the present cases such that a geometric mean remains smaller than $\Delta z(z)$.

We have also compared our SEM results with a FDM code and find excellent agreement for global quantities such as Nusselt number and temperature profiles, and even fair agreement with globally averaged dissipation rates. The only discrepancy is with the vertical profiles of the mean dissipation rates, which disagree by about 9%.

Once we determined our resolution criteria, we then compared local dissipation rates (ϵ, ϵ_T) and the local dissipation scale η_k as a function of Rayleigh number for our sufficiently resolved simulations. Local dissipation scales can be considered as a generalization of the mean Kolmogorov dissipation scale which incorporate the spatially intermittent nature of the energy dissipation field. Local scales below the Kolmogorov scales are related to strong local gradients or high-amplitude dissipation events. We find that the local dissipation scales in the entire cell have a wider range of values than the dissipation scales in the bulk of the cell.

But in all cases, there is a fairly wide range of dissipation scales both above and below the mean Kolmorgov dissipation scale. The range of these local scales is a manifestation of the intermediate dissipation range (IDR) which exists in the crossover region between the inertial and viscous range. The IDR was developed in the multifractal formalism [4, 13, 19, 20]. Similar to previous studies in box turbulence and channel flow turbulence, this range increases as the Rayleigh number grows. We have shown here that the dissipation scales on the left end of the PDFs become smaller as Rayleigh number increases, and correspondingly the probability of largest dissipation scales decreases. We also found, by looking at the fourth moment of the thermal dissipation rate, that high-amplitude but rare dissipation events can dominate the tails of the PDFs of the thermal dissipation rates. This highlights the sensitivity of turbulent RBC to such rare, but extreme events and calls for caution when generalizing statistical quantities in turbulent RBC. We also computed the joint statistics of the kinetic energy and thermal dissipation rates and find that the high amplitude events are the most strongly correlated.

Finally we compared results at two different Prandtl numbers. The range of local dissipation scales becomes smaller when $Pr > 1$ which is in line with smaller amplitudes of both dissipation rates. Our estimates (18) indicate that the resolution demands grow significantly when the Prandtl number is decreased starting from $Pr \approx 1$. Equation (18) suggests a stronger Prandtl number dependence on the dissipation scales, namely $\langle \eta_K \rangle \sim Pr^{3/8}$, for cases decreasing from $Pr \approx 1$ to $Pr \ll 1$ than for those which increase from $Pr \approx 1$ to $Pr \gg 1$ (where $\langle \eta_B \rangle \sim Pr^{-1/8}$). On the numerical side, a second challenge appears that is related to the high diffusivity of temperature field and which has been discussed recently for the case of passive scalar mixing at very low Schmidt number [40]. An explicit time advancement becomes increasingly demanding since the scalar relaxes increasingly faster. Preliminary studies suggest e.g. that for the Prandtl number of mercury ($Pr = 0.021$) a mesh is necessary that equals the one which we used for $Pr = 0.7$ for a Rayleigh number larger by a factor of one hundred.

Acknowledgments

First, we would like to thank Paul F Fischer for his continuous help in getting the nek5000 spectral element software package optimized and adapted to our RBC problem. JS thanks the Deutsche Forschungsgemeinschaft for financial support within the Research Unit FOR 1182 and the German–Israeli–Foundation with grant 1072-6.14/2009. Supercomputing resources on Blue Gene/Q Juqueen at the Jülich Supercomputing Centre have been obtained within Grant HIL07 which has been selected as a large-scale project in the German Gauss Centre for Supercomputing. We thank them for this steady support of our work. JDS acknowledges also an INCITE director's discretionary allocation for Blue Gene/P Intrepid and Blue Gene/Q Mira at Argonne National Laboratory. The work benefited from discussions with Bruno Eckhardt, Roberto Verzicco and Katepalli R Sreenivasan.

Appendix. Additional resolution studies

A.1. Sensitivity with respect to vertical element spacing

In this section, we describe in brief one way to obtain an optimal scaling factor r given by (27). As r becomes smaller, the elements become more clustered toward the boundary plates as shown in figure A.1. Table A.1 summarizes ten different test runs at fixed Ra, Pr and Γ. In all cases

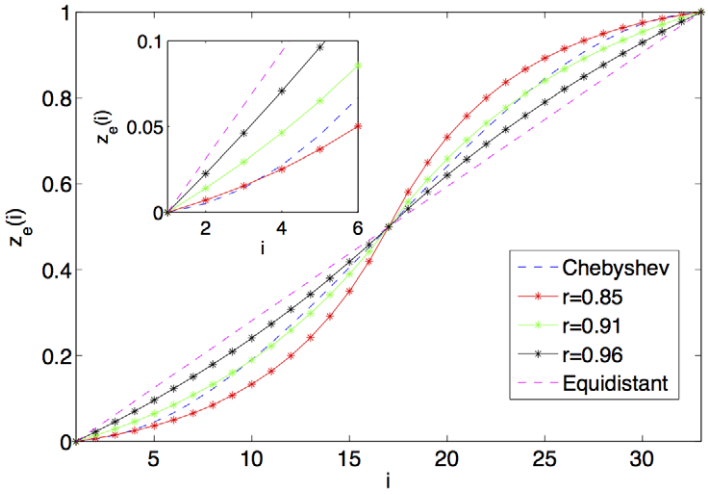

Figure A.1. Display of the vertical primary node structure with $N_{e,z} = 32$, where $i = 1 \ldots N_{e,z} + 1$ and $z_e(i) \in [0, 1]$. The geometric scaling factor r causes different narrow node spacings in the vicinity of the top and bottom plate. For visual comparison we add an equidistant spacing and the Chebyshev collocation points. The inset displays a zoom into the vicinity of the bottom plate.

the horizontal mesh (see again figure 1) and the total number of elements N_e remain unchanged. We varied the polynomial order N and r only.

Figure A.2 shows time series of the Nusselt numbers for the different values of r obtained at $z = 0$, i.e. $Nu(t) = -\partial\langle T\rangle_A/\partial z|_{z=0}$. The values $Nu(t)$ fluctuate about their temporal means. These fluctuations do not decrease when N is increased, i.e. when the resolution is improved (not shown). A systematic effect for an increase of r is clearly visible in the insets of both figures, where we report the time averages of $Nu(t)$ at both plates with the error bars corresponding to the standard deviation σ. Neither an equidistant nor a strongly non-uniform grid are preferable since they give the largest discrepancy in Nusselt number. There is a trade-off between resolving the boundary layers (non-uniform grid) and the bulk (equidistant grid). Based on our analysis here, scaling factors of about $r \approx 0.9$ seem to be the optimum and were kept for the rest of the studies. For the present studies, we have chosen $r = 0.91$ and have also matched finer primary element meshes correspondingly.

A.2. Complementary series of resolution tests

A complementary series of resolution tests in comparison to those reported in section 3.1 is presented in table A.2 and figure A.3. In the test runs T11 to T13 we varied the primary element meshes and left the polynomial order of each element unchanged. The outcome from this series is similar to what was already demonstrated in the main text. While the vertical profiles for the mean temperature or the mean convective heat flux are practically equal, differences manifest for the gradient fields (see figure A.3 for details).

A.3. Spatial derivatives in the spectral element method

In order to illustrate how we take very accurate derivatives in the SEM, we use as an example a one-dimensional case with the reference element $\Omega = [-1, 1]$. A spectral approximation of a

Table A.1. Parameters of the different spectral element test runs T1–T10 with different vertical spacing. We display the order N of the Legendre polynomials, the geometric stretching factor r in the vertical direction, the total number of spectral elements, N_e, the number of spectral elements with respect to z direction, $N_{e,z}$ and the number of grid cells resulting from primary and secondary nodes with respect to z direction, $N_z = N_{e,z}N$. In all cases, $Ra = 10^9$, $\Gamma = 1$ and $Pr = 0.7$.

Run	N	r	N_e	$N_{e,z}$	N_z
T1	3	0.85	30 720	32	96
T2	5	0.85	30 720	32	160
T3	3	0.88	30 720	32	96
T4	5	0.88	30 720	32	160
T5	3	0.91	30 720	32	96
T6	5	0.91	30 720	32	160
T7	3	0.93	30 720	32	96
T8	5	0.93	30 720	32	160
T9	3	0.96	30 720	32	96
T10	5	0.96	30 720	32	160

function $u_e \in L^2_w(\Omega)$ (with $w(x)$ being a positive weight function) can be written as follows

$$u_e(x) = \sum_{k=0}^{N} u(\xi_k)\psi_k(x), \tag{A.1}$$

where $\psi_k(x)$ is the kth order basis function and the (N+1) points are the nodes of the Gauss–Lobatto quadrature. They are determined by the Gauss–Lobatto integration theorem [6]. For the approximation, one has to take a set of polynomials which form an orthogonal system of the underlying Hilbert space of square-integrable functions $L^2_w(\Omega)$.

The first derivative of the function $u_e(x)$ at the GLL points is

$$D_e u(\xi_k) = \sum_{j=0}^{N} u(\xi_j) \frac{\mathrm{d}\psi_j(x)}{\mathrm{d}x}\bigg|_{x=\xi_k}. \tag{A.2}$$

Starting from equation (23) together with the relation $(1-x^2)L'_N(x) = 0$ for $x = \xi_k$ and substituting the Legendre differential equation $((1-x^2)L'_N(x))' = -N(N+1)L_N(x)$ the derivative becomes

$$\frac{\mathrm{d}\psi_j(x)}{\mathrm{d}x}\bigg|_{x=\xi_k} = \begin{cases} \dfrac{L_N(\xi_k)}{(\xi_k - \xi_j)L_N(\xi_j)} & \text{if } \xi_k \neq \xi_j, \\ \dfrac{N(N+1)}{4} & \text{if } k = j = N, \\ -\dfrac{N(N+1)}{4} & \text{if } k = j = 0, \\ 0, & \text{otherwise.} \end{cases} \tag{A.3}$$

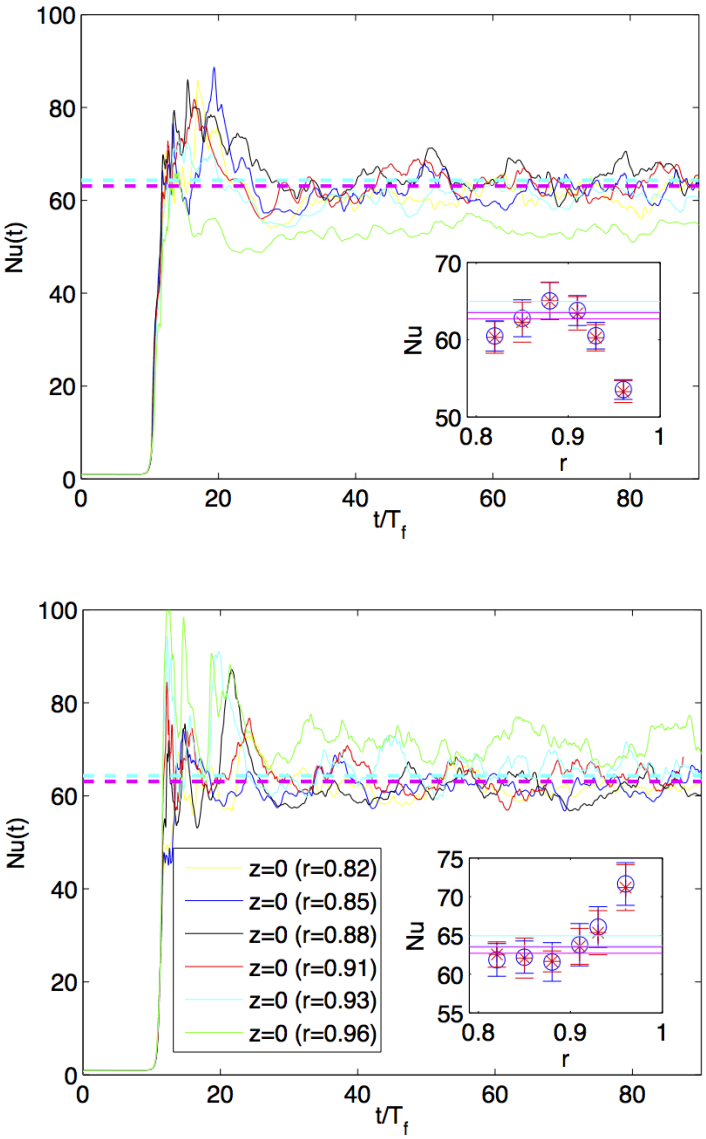

Figure A.2. Nusselt number at $z = 0$ versus time. Results at differently stretched vertical grids are shown. The dashed lines show the reference values of Nu from other DNS: cyan dashed line for a run at same Ra from [2] and the magenta dashed line from [35]. The number of elements is the same in both series. Top: polynomial order $N = 3$ with runs T1, T3, T5, T7 and T9. Bottom: $N = 5$ with runs T2, T4, T6, T8 and T10. The insets in both figures display Nu as obtained by a time average at $z = 0$ (blue circles) and 1(red stars) as well as the corresponding error bars. For comparison we add again $Nu \pm \sigma$ from [2, 35] in the same color style as in the main figures. All data are for $Ra = 10^9$ and $\Gamma = 1$ (see table A.1).

We also recall that $L_N(-1) = (-1)^N$ and $L_N(1) = 1$ for all N. Thus, the derivative at the boundary $x = \xi_0$ is given by

$$D_e u(\xi_0) = -\frac{N(N+1)}{4} u(\xi_0) + \sum_{j=1}^{N} \frac{u(\xi_j)(-1)^N}{(\xi_0 - \xi_j) L_N(\xi_j)} \tag{A.4}$$

Table A.2. Parameters of the different spectral element simulations T11–T13. The three runs have different primary node meshes, but the same polynomial order $N = 7$. We display the order N of the Legendre polynomials, the total number of spectral elements, N_e, the number of spectral elements with respect to z direction, $N_{e,z}$, the number of grid cells resulting from primary and secondary nodes with respect to z direction, $N_z = N_{e,z}N$ and the Nusselt numbers $Nu(z = 0)$, $Nu(z = 1)$ and Nu_V. Furthermore we list the relative errors Λ_T and Λ_v (see equations (19)). All runs are at $Ra = 10^9$, $\Gamma = 1$ and $Pr = 0.7$. Note that T13 equals SEM9.

Run	N	$(N_e, N_{e,z})$	N_z	$Nu(0) \pm \sigma$	$Nu(1) \pm \sigma$	$Nu_V \pm \sigma$	Λ_T	Λ_v
T11	7	(30720, 32)	96	61.8 ± 1.0	61.8 ± 1.1	63.1 ± 2.4	1.7%	4.0%
T12	7	(256000, 64)	448	62.8 ± 1.0	62.6 ± 1.1	62.9 ± 4.7	0.4%	0.2%
T13	7	(875520, 96)	672	62.8 ± 2.0	62.9 ± 2.3	62.8 ± 5.0	0.1%	0.1%

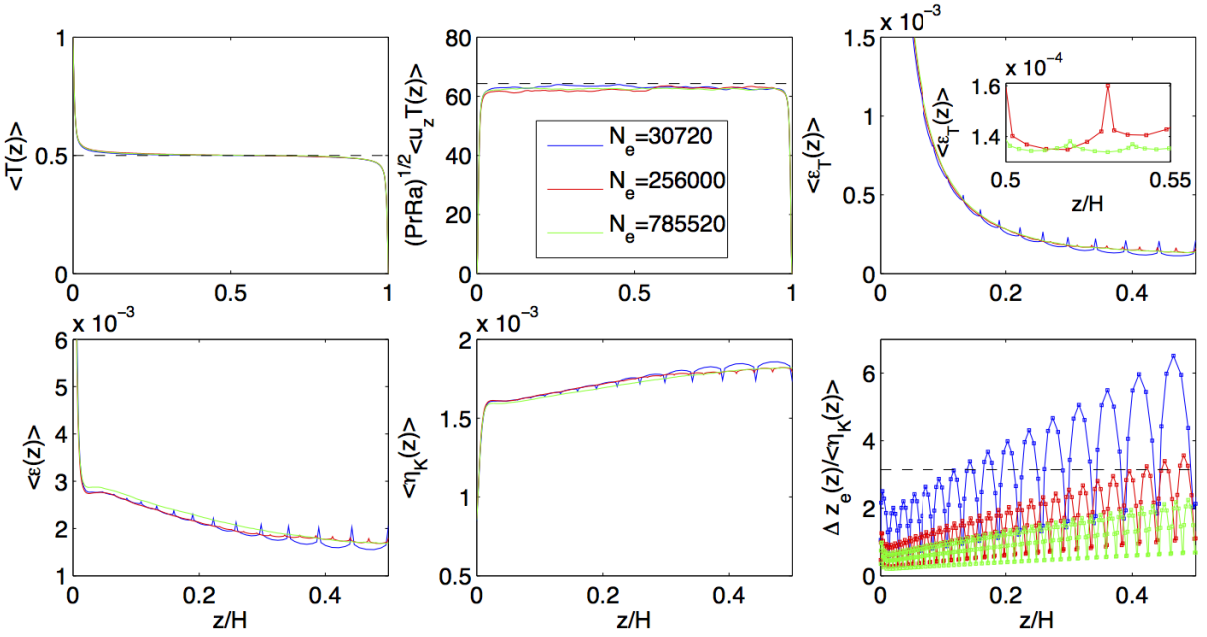

Figure A.3. Resolution tests for $Ra = 10^9$, $\Gamma = 1$ and $N = 7$ using different primary meshes (runs T11–T13 in table A.1). We compare the same quantities as in figure A.2. The dashed line in the lower right panel marks $\Delta z_e(z)/\eta_K(z) = \pi$. The dashed line in the upper mid panel is the Nusselt number from run FDM1 as displayed in table 2.

at $x = \xi_k$ for $0 < k < N$ by

$$D_e u(\xi_k) = \sum_{\substack{j=0 \\ j \neq k}}^{N} \frac{u(\xi_j) L_N(\xi_k)}{(\xi_k - \xi_j) L_N(\xi_j)}, \tag{A.5}$$

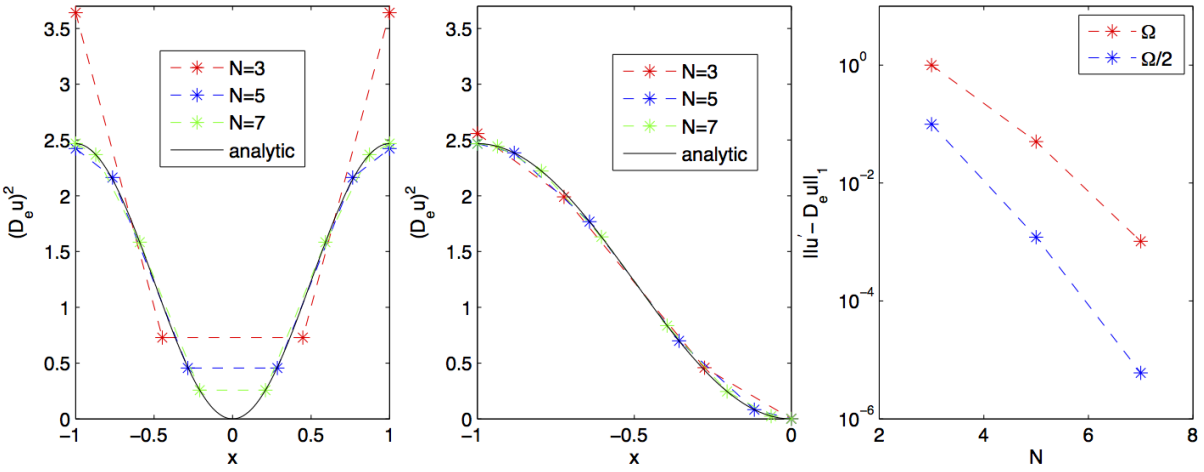

Figure A.4. First-order derivative as a function of polynomial order and element size. Left: the results for $(\mathrm{d}u/\mathrm{d}x)^2$ where $u(x) = \cos(\pi x/2)$ with $x \in [-1, 1]$ are displayed. Mid: same results but for an primary element mesh $(\Omega/2)$ twice as fine as in the left figure (Ω). Right: exponential convergence of the error as defined in (A.7).

and at $x = \xi_N$ by

$$D_e u(\xi_N) = \sum_{j=0}^{N-1} \frac{u(\xi_j)}{(\xi_N - \xi_j) L_N(\xi_j)} + \frac{N(N+1)}{4} u(\xi_N). \tag{A.6}$$

In figure A.4 we summarize the results for a simple function $u(x) = \cos(\pi x/2)$. With a view to dissipation rates we are interested in the accuracy for quantities that contain $(\mathrm{d}u/\mathrm{d}x)^2$. In the left panel of figure A.4, we compare the derivative as obtained from (A.4)–(A.6). We see that the errors at the boundary result in strong overshoots at the element boundary which are amplified by the second power of the derivatives as in the dissipation rates. The mid panel of figure A.4 repeats the analysis for a primary element node mesh of half the size obtained here by $\tilde{x} \to (x-1)/2$. An increase in resolution of the primary element node mesh reduces the errors significantly. The error can be quantified by

$$\| u' - D_e u \| = \sum_{j=0}^{N} |u'(\xi_j) - D_e u(\xi_j)|, \tag{A.7}$$

which is shown in the right panel of figure A.4. The exponential convergence with respect to the polynomial order N is clearly demonstrated in the right panel of the figure. Thus a combination of both increasing the polynomial order and the node mesh leads to an accurate calculation of spatial moments.

References

[1] Ahlers G, Grossmann S and Lohse D 2009 Heat transfer and large scale dynamics in turbulent Rayleigh–Bénard convection *Rev. Mod. Phys.* **81** 503–37

[2] Bailon-Cuba J, Emran M S and Schumacher J 2010 Aspect ratio dependence of heat transfer and large-scale flow in turbulent convection *J. Fluid Mech.* **655** 152–73

[3] Batchelor G K 1959 Small scale variation of convected quantities like temperature in a turbulent fluid *J. Fluid Mech.* **5** 113–33
[4] Biferale L 2008 A note on the fluctuations of dissipation scale in turbulence *Phys. Fluids* **20** 031703
[5] Chillà F and Schumacher J 2012 New perspectives in turbulent Rayleigh–Bénard convection *Eur. J. Phys.* E **35** 58
[6] Deville M O, Fischer P F and Mund E H 2002 *High-Order Methods for Incompressible Fluid Flow* (Cambridge: Cambridge University Press)
[7] Emran M S and Schumacher J 2008 Fine-scale statistics of temperature and its derivatives in convective turbulence *J. Fluid Mech.* **611** 13–34
[8] Emran M S and Schumacher J 2012 Conditional statistics of thermal dissipation rate in turbulent Rayleigh–Bénard convection *Eur. J. Phys.* E **35** 108
[9] http://nek5000.mcs.anl.gov
[10] Fischer P F 1997 An overlapping Schwarz method for spectral element solution of the incompressible Navier–Stokes equations *J. Comp. Phys.* **133** 84–101
[11] Fischer P F and Mullen J 2001 Filter-based stabilization of spectral element methods *C. R. Acad. Sci.* **332** 265–70
[12] Fischer P F, Lottes J W, Pointer D and Siegel A 2008 Petascale algorithms for reactor hydrodynamics *J. Phys. Conf. Ser.* **125** 012076
[13] Frisch U and Vergassola M 1991 A prediction of the multifractal model—the intermediate dissipation range *Europhys. Lett.* **14** 439–44
[14] Hamlington P E, Krasnov D, Boeck T and Schumacher J 2012 Local dissipation scales and energy dissipation-rate moments in channel flow *J. Fluid Mech.* **701** 419–29
[15] Hamlington P E, Krasnov D, Boeck T and Schumacher J 2012 Statistics of the energy dissipation rate and local enstrophy in turbulent channel flow *Physica* D **241** 169–77
[16] Grötzbach G 1983 Spatial resolution requirements for direct numerical simulation of the Rayleigh–Bénard convection *J. Comput. Phys.* **49** 241–64
[17] Kaczorowski M and Xia K-Q 2013 Turbulent flow in the bulk of Rayleigh–Bénard convection: small-scale properties in a cubic cell *J. Fluid Mech.* **722** 596–617
[18] Mellado J P 2010 The evaporatively driven cloud-top mixing layer *J. Fluid Mech.* **660** 5–36
[19] Nelkin M 1990 Multifractal scaling of velocity derivatives in turbulence *Phys. Rev.* A **42** 7226–9
[20] Paladin G and Vulpiani A 1987 Degrees of freedom of turbulence *Phys. Rev.* A **35** 1971–3
[21] Scheel J D, Kim E and White K R 2012 Thermal and viscous boundary layers in turbulent Rayleigh–Bénard convection *J. Fluid Mech.* **711** 281–305
[22] Schumacher J, Yeung P K and Sreenivasan K R 2005 Very fine structures in scalar mixing *J. Fluid Mech.* **531** 113–22
[23] Schumacher J 2007 Sub-Kolmogorov scale fluctuations in fluid turbulence *Europhys. Lett.* **80** 54001
[24] Schumacher J, Sreenivasan K R and Yakhot V 2007 Asymptotic exponents from low-Reynolds-number flows *New J. Phys.* **9** 89
[25] Schumacher J, Eckhardt B and Doering C R 2010 Extreme vorticity growth in Navier–Stokes turbulence *Phys. Lett.* A **374** 861–5
[26] Shi N, Emran M S and Schumacher J 2012 Boundary layer structure in turbulent Rayleigh–Bénard convection *J. Fluid Mech.* **706** 5–33
[27] Shishkina O, Stevens R A J M, Grossmann S and Lohse D 2010 Boundary layer structure in turbulent thermal convection and its consequences for the required numerical resolution *New J. Phys.* **12** 075022
[28] Shraiman B I and Siggia E D 1990 Heat transport in high-Rayleigh-number convection *Phys. Rev.* A **42** 3650–3
[29] Sreenivasan K R and Antonia R A 1997 The phenomenology of small-scale turbulence *Annu. Rev. Fluid Mech.* **29** 435–72
[30] Sreenivasan K R 2004 Possible effects of small-scale intermitency in turbulent reacting flows *Flow Turbul. Combust.* **72** 115–32

[31] Stevens R A J M, Verzicco R and Lohse D 2010 Radial boundary layer structure and Nusselt number in Rayleigh–Bénard convection *J. Fluid Mech.* **643** 495–507
[32] Tufo H M and Fischer P F 2001 Fast parallel direct solvers for coarse grid problems *J. Parallel Distrib. Comput.* **61** 151–77
[33] Verzicco R and Orlandi P 1996 A finite-difference scheme for three-dimensional incompressible flows in cylindrical coordinates *J. Comput. Phys.* **123** 402–14
[34] Verzicco R and Camussi R 2003 Numerical experiments on strongly turbulent thermal convection in a slender cylindrical cell *J. Fluid Mech.* **477** 19–49
[35] Wagner S, Shishkina O and Wagner C 2012 Boundary layers and wind in cylindrical Rayleigh–Bénard cells *J. Fluid Mech.* **697** 336–66
[36] Wallace J M 2009 Twenty years of experimental and direct numerical simulation access to the velocity gradient tensor: What have we learned about turbulence? *Phys. Fluids* **21** 021301
[37] Watanabe T and Gotoh T 2004 Statistics of a passive scalar in homogeneous turbulence *New J. Phys.* **6** 40
[38] Yakhot V and Sreenivasan K R 2005 Anomalous scaling of structure functions and dynamic constraints on turbulence simulations *J. Stat. Phys.* **121** 823–41
[39] Yakhot V 2006 Probability densities in strong turbulence *Physica* D **215** 166–74
[40] Yeung P K and Sreenivasan K R 2013 Spectrum of passive scalars of high molecular diffusivity in turbulent mixing *J. Fluid Mech.* **716** R14
[41] Zhou Q and Xia K-Q 2010 Universality of local dissipation scales in buoyancy-driven turbulence *Phys. Rev. Lett.* **104** 124301